Fatigue life extension using composite patch repairs

by

Preben Brekke Rotwitt

Thesis for the degree of

MASTER OF SCIENCE

(Master i Anvendt matematikk og mekanikk)

Faculty of Mathematics and Natural Sciences

University of Oslo

May 2013

Det matematisk-naturvitenskapelige fakultet
Universitetet i Oslo

Preface

The present thesis is submitted as part of the requirements for a master degree in Solid Mechanics, a specialization of the master program Applied Mathematics and Mechanics, at the Faculty of Mathematics and Natural Sciences, University of Oslo.

The project has been performed in collaboration with Det Norske Veritas (DNV).

I wish to offer my gratitude to my supervisors, Professor Brian Hayman at the University of Oslo and Principal Engineer Jan Weitzenböck at DNV for their guidance and support. I would also like to thank Arne Fjeldstad at DNV for his guidance, my fellow students for motivation and helpful discussions, Lars K. Rødbakk for proofreading and Malene H. Rødbakk for her support.

Blindern, May 2013

Preben Brekke Rotwitt

Contents

Terms, symbols and definitions

LEFM	Linear elastic fracture mechanics
SL joint	Single lap joint
DL joint	Double lap joint
SBS joint	Single butt strap joint
DBS joint	Double lap joint
CFRP	Carbon fibre reinforced polyester
GFRP	Glass fibre reinforced polyester
GFRE	Glass fibre reinforced epoxy
FPSO	Floating production, storage and offloading unit
FSO	Floating storage and offloading unit
SENT	Single-edge notched tension
A	Crack area
a	Crack length
a_c	Critical crack length
a_f	Final crack length
a_i	Initial crack length
a_y	Corresponding crack length to fully plastic yielding
C, m	Material constants in Paris Power Law
E	Young's Modulus
E_0	Young's Modulus of the overlap (or outer adherend)
E_s	Young's Modulus of the substrate
E_i	Young's Modulus of the inner adherend
F	Stress intensity correction factor (or Externally applied load)
F_{max}	Externally applied failure load
F_f	*F* factor corresponding to a_f
F_i	*F* factor corresponding to a_i
G_a	Shear modulus in the adhesive

G_o	Shear modulus in the overlap (or outer adherend)
G_i	Shear modulus in the inner adherend
h	Plate half height
$\bar{J}$	*J*-Contour Integral
K	Stress intensity factor
K_I	Mode I loading stress intensity factor
K_{II}	Mode II loading stress intensity factor
K_{III}	Mode III loading stress intensity factor
K_c	Critical stress intensity factor, or fracture toughness
K_{nn}	Elastic element tensile stiffness for pure Mode I fracture with cohesive elements
K_{ss}	Elastic element shear stiffness for pure Mode II fracture with cohesive elements
K_{tt}	Elastic element shear stiffness for pure Mode III fracture with cohesive elements
l	Length of bondline
L_O	Overlap length
L_S	Steel plate length
N	Fatigue cycles
N_{if}	Fatigue cycles needed for a crack to propagate from a_i to a_f
R	Stress ratio (S_{min}/S_{max})
r	Radial distance from crack tip
S	Applied stress
s_n^o	Nominal tensile damage initiation traction for Mode I fracture
s_s^o	Nominal shear damage initiation traction for Mode II fracture
s_t^o	Nominal shear damage initiation traction for Mode III fracture
t_a	Thickness of adhesive layer
t_i	Thickness of the inner adherend
t_0	Thickness of the overlap (outer adherend)
t_s	Thickness of the substrates (or steel plate)
W_O	Overlap witdh
W_S	Steel plate width
α	Ratio of crack length and plate width

Γ	Energy release rate
Γ_c	Critical energy release rate
Γ_{cn}	Critical energy release rate for Mode I fracture
Γ_{cs}	Critical energy release rate for Mode II fracture
Γ_{ct}	Critical energy release rate for Mode III fracture
τ_x	Shear stress in the adhesive bondline
τ_y	Yield shear stress in the adhesive bondline
Π	Potential energy of an elastic body
x	Distance along the bondline, measured from the center of the adhesive
ΔK	Stress intensity range
ΔS	Stress range

Chapter 1

Introduction

1.1 General background

According to R. D. Adams “an adhesive can be defined as a polymeric material which, when applied to surfaces, can join them together and resist separation” (Adams, et al., 1997).

The origin and history of these adhesive materials are uncertain. Writings and archaeological evidence suggest, however, that humans have been using adhesives for thousands of years. In the beginning adhesives were mostly used in the making of simple tools and weapons for hunting and fighting. Later, its area of application included, among others, artwork and construction.

The history of manufactured adhesives appears to have started long before the existence of modern humans. In 1963, Neanderthal tools dating from at least 80 000 years ago were found in Germany. The tools had residues of an adhesive substance derived from processed birch pitch. Similarly, tools dating from around 40 000 BC, found in Syria, used bitumen as a hafting material joining the tools to their handles (Adams, et al., 2005).

Since the days of the Neanderthals, manufacturing and the area of use for adhesive materials has evolved a great deal. Today adhesive bonding is used in a wide range of applications from advanced air- and watercrafts to simple household products. Some classic examples are the Fokker F50 and Lotus Elise, both manufactured with extensive use of adhesive bonding.

The reasons for choosing adhesive bonding are multiple. Adhesive bonding has some other characteristics and benefits compared to joining methods as bolting, riveting and welding. Because of this, there are some situations where adhesive bounding is favourable. Typical are for the assembly of lightweight structures based on thin materials or material combinations such as composite and steel that cannot be welded. There can also be requirements for smooth surfaces or safety reasons for choosing adhesive bonding, such as avoiding hot work and the risk of fire.

No joining process comes without weaknesses and adhesive bonding does also have some disadvantages. Some of the pros and cons of adhesive bonding are listed in the table below.

Table 1.1: Characteristic features of adhesive joints

Advantages	Disadvantages
• Uniform stress distribution (avoids drilled holes and stress concentrations). • Provides a large stress-bearing area. • Joins materials of all shapes and thicknesses. • Possibility to join different materials. • High dynamic strength. • Good damping properties. • Provides excellent fatigue strength. • Minimizing or prevent galvanic corrosion between dissimilar metals. • Provide smooth contours. • Seal joints (gas-proof and liquid-tight). • Avoids hot work. • Provide attractive strength-to-weight ratio.	• Cleaning and surface preparation of the adherents is necessary in many cases. • Long cure time may be needed. • Heat and pressure may be required for cure. • Rigid process control usually necessary. • Cannot measure adhesion strength non-destructively. • Can be affected by environmental factors as heat and moisture.

1.1.1 Uses of adhesives in the maritime industry

There are a number of actual and potential applications for adhesive bonding in the maritime industry. Many applications are and have been related to the superstructure of a ship. For instance the use of adhesives bonding to repair cracks in aluminium superstructures and to join lightweight structures made of composite or aluminium to the steel hull. It is anticipated that in order to save weight and hence reduce fuel costs, the use of lightweight and hybrid materials will become more widespread (Weitzenböck, 2012).

In the later years there has also been an increased interest in the use of composite repair solutions for repairs of steel structures. Steel plates and pipes in ships and other offshore structures are often operating in harsh environmental conditions. These challenging conditions can result in a variety of damage scenarios, including coating damage, erosion, corrosion or mechanical damage. Two of the most common scenarios experienced by the maritime industry are internal and/or external corrosion and fatigue related problems. Depending on the severity, these problems can have a significant negative effect on the pressure bearing capabilities and structural capacity of the steel structure and may consequently lead to reduced lifespan or failure. Traditionally load bearing capabilities have been restored by welding or by replacing the damaged pipe/plate, but these methods of mending do have some limitations and may entail some challenges. Access in many cases may be problematic.

The damaged parts are often located in closed compartments, making them hard to replace. Performing hot work on a ship or an offshore installation may also involve explosion or fire hazard and a shutdown of normal operation is often necessary.

Composite repair solutions offer an alternative to conventional methods. A recent approach to repairing damage plates is *composite patch repair*. A composite patch is adhesively bonded over a defect area in order to restore the load carrying capacity of the structure. The patch transfers loads around the defect and stops the defect from growing. The composite patch can be applied "in situ" without the use of hot work, hence eliminating the explosion hazard. The method can be especially favourable in the oil and gas industry where cold joining processes can minimize the impact of maintenance work or modifications due to the reduced danger of explosions (Weitzenböck, 2012). The repairs may be used as a temporary solution until scheduled maintenance may be performed.

The principle of composite patch repair is illustrated in Figure 1.1.

Figure 1.1: Composite patch repair of a damage area

Due to the increasing interest in the use of adhesive bounding and composite patch repair, there is a need for reliable capacity models and documentation that states that these repairs in fact restores the load bearing capabilities of the mended structures.

Motivated by this fact, "Det Norske Veritas" in collaboration with a student at the University of Oslo (Guthu, 2010) has recently performed studies that have resulted in a promising model for strength predictions of bonded joints. In this thesis, that numerical model will be adapted to examine how composite patches can reduce fatigue crack propagation in cracked steel plates.

1.2 Organisation of the thesis

The present thesis starts with an introduction to the most relevant fracture mechanics theory, with emphasis on the stress intensity factor and fatigue crack growth. The following chapter presents a brief introduction to the theory of adhesively bonded joints.

In Chapter 4, a proved well-functioning finite element model of a double butt strap joint with cohesive elements will be remodelled and adapted into a three-dimensional single-edge notched tension (SENT) steel plate with CFRP reinforcements. The objective of the modelling is to successfully analyse the stress intensity at the crack tip, with and without CFRP patches, and to perform a parametric study investigating the patches ability to reduce the stress intensity.

In Chapter 5, a ship manhole experiencing fatigue crack growth is modelled with two patch repair alternatives. The main objective of the modelling is to study fatigue crack growth and to perform life estimates for configurations with and without CFRP patches.

In Chapter 6, results from the analyses will be presented and discussed.

At last, conclusions regarding the performance of the patches will be drawn.

1.3 Redefinition of the thesis

The first project description was presented January 21. The main objective of this thesis was to model and study composite repairs of pipes on board ships and offshore floating structures by the use of cohesive elements. The main interest was non-standard geometries for pipe repairs and to study the effect of over-laminating of pipe-flanges for composite wrap repair.

The plan was to start with straight pipe sections and then extend the modelling to non-standard end connections, as pipe to bulkhead and pipe to sideshell.

To perform the studies, test results were needed in order to calibrate the cohesive elements for mixed mode fracture. The test results DNV had at their disposal turned out, however, to be inadequate. Performing the planned activities was, consequently, impossible.

Defining a new assignment took some time and a new outline for the MSc project was not in place until March 13, it was then decided that the thesis should focus on fatigue crack growth in steel plates and how crack growth can be limited by the use of composite patches.

The problems related to the shuttle tanker (see Chapter 5) were not presented until April 4.

Due to the circumstances and the limited amount of time that has been available, the scope of the present thesis is to some extent reduced.

Chapter 2

Fracture mechanics

Fracture mechanics is the field of mechanics concerned with the study of propagation of cracks in materials. The presence of imperfections such as cracks in structures may weaken the structure so that it fails by fracturing. This can occur even though stresses are well below the material yield strength. Cracks or cracklike flaws occur frequently in structures such as bridges, pressure vessels, piping, aircrafts, heavy machinery and ships, and so the study and use of fracture mechanics is of major engineering importance.

Minor cracks in vital structures can have fatal consequences and have been the cause of several deadly accidents. One example was the British-made Comet passenger airliner, two of which failed at high altitude in the 1950s, with considerable loss of life in the resulting crashes (Dowling, 2012). Such failures accelerated the development of fracture mechanics, and the incident (or rather incidents) that may have had greatest impact was the failure of the Liberty ships. According to Anderson, the mechanics of fracture progressed from being a scientific curiosity to an engineering discipline, primarily because of the design of the Liberty ships during the World War II (Anderson, 2005).

The solution for Britain's great need for supply ships was the U.S. built Liberty ships. The ships were manufactured with a revolutionary new procedure. The vessels had an all-welded hull, as opposed to the riveted construction of traditional ship designs. The new construction method reduced labour costs and construction time.

The Liberty ship program was an unquestionable success, until one day in 1943, when one of the vessels completely broke in two and sank in the Bering Sea. Subsequent fractures occurred in other Liberty ships. Of the roughly 2700 Liberty ships built during World War II, approximately 400 sustained fractures, of which 90 were considered serious. On 20 ships the failure was essentially total, and about half of these completely broke in two (Anderson, 2005).

It was later determined that the Liberty ship failures were caused by a combination of three factors:

- The welds, which were produced by a semi-skilled work force, contained crack-like flaws.
- Most of the fractures initiated on the deck at square hatch corners, where there was a local stress concentration.
- The steel from which the Liberty ships were made had poor fracture toughness.

The steel in question had always been adequate for riveted ships because fracture could not propagate across panels that were joined by rivets. Because of the welded structure, propagating cracks in the Liberty ships encountered no significant barriers, and were sometimes able to traverse the entire hull.

Once the causes of failure were identified, the remaining Liberty ships were refitted with rounded reinforcements at the hatch corners. In addition, crack-arrester plates of high toughness steel were riveted to the deck at strategic locations. These corrections prevented further serious fractures.

The investigations and research following the Liberty accidents was the start of the field we now know as fracture mechanics.

In the following sections relevant fracture mechanics theory will be discussed and the two main approaches to fracture analysis will be presented; the energy approach and the stress-intensity approach.

2.1 Stress concentration effect of cracks

Most of the fractures that occurred on the Liberty ships emanated from square hatch corners in the deck. The reason for this was local stress concentrations around the corners. All openings in a ship deck will cause stress concentrations, on the Liberty ships these stress concentrations were intensified by the sharp corners of the hatches, which led to the development of cracks.

The stress raising effect of sharp corners or a sharp crack can be explained by considering an infinite wide plate with an elliptical hole in the plate's centre, as illustrated in Figure 2.1. The plate is loaded with a uniform tension stress, S. The local stress that is parallel to the applied stress, σ_y, will at a far distance from the hole be equal to the applied stress, S, but the value of σ_y will increase sharply near the hole and reach a maximum at the edge of the hole, at the tip of the crack. The magnitude of the stress concentration at the edge of the hole depends on the hole's proportions and the crack tip radius ρ.

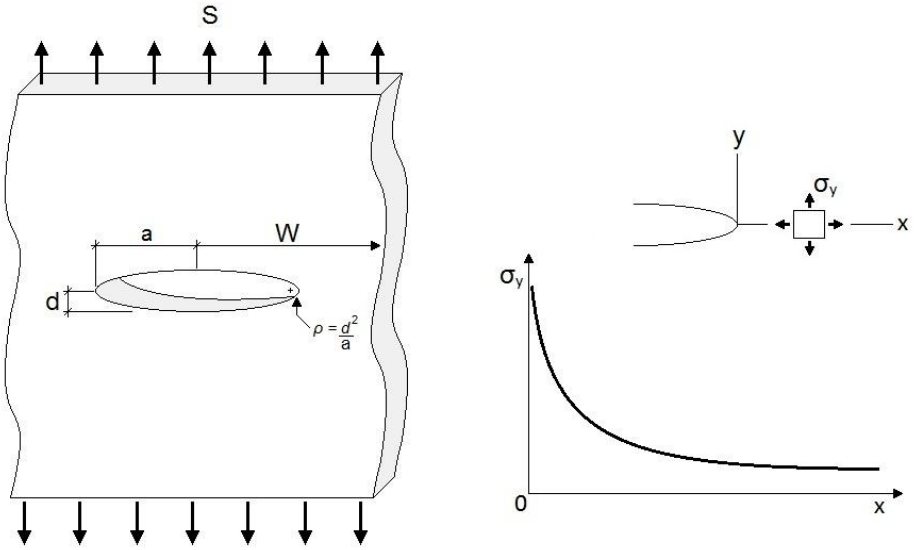

Figure 2.1: Elliptical hole in an infinite wide plate experiencing remote uniform tension, and the stress distribution along the x-axis near the hole.

The maximum value of σ_y can be expressed in the following way:

$$\sigma_y = S\left(1 - \frac{2a}{d}\right) = S\left(1 + 2\sqrt{\frac{a}{\rho}}\right) \tag{2.1}$$

As we can see from Equation (2.1), a smaller crack tip radius leads to a larger stress concentration. When the half-height *d* of the ellipse approaches zero, so that the crack tip radius *ρ* also approaches zero, σ_y becomes infinite. Hence, a sharp slit like crack causes a severe concentration of stress that is theoretically infinite if the crack is ideally sharp (Dowling, 2012). However, infinite stress cannot exist in a real material. In ductile materials, the material will experience plastic deformations in the area surrounding the crack tip, the *plastic zone*. Yielding of the material in the plastic zone results in the sharp crack tip being blunted to a small, but nonzero, radius. Hence, reducing the stress to a finite level and creating a so called *crack-tip opening displacement* (CTOD), δ. This is illustrated in Figure 2.2.

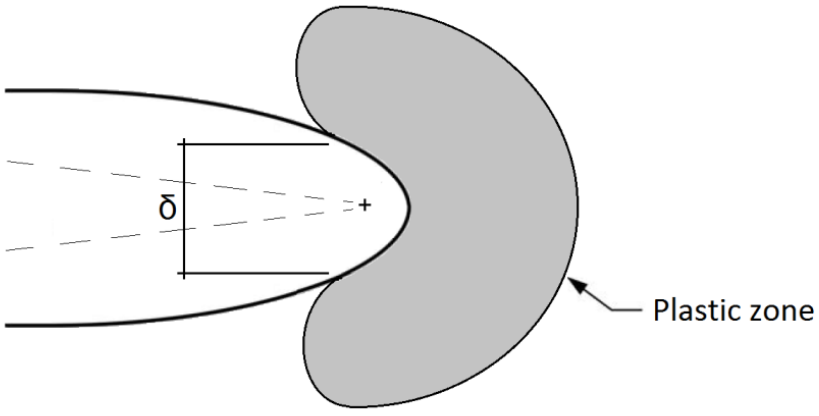

Figure 2.2: Plastic deformation of crack tip.

2.1.1 Effect of finite size

The stress concentration at a crack tip are not only controlled by the crack tip radius, but is also influenced by external boundaries. As the crack size increases, or as the plate dimensions decrease, the outer boundaries begin to exert an influence on the crack tip.

Consider a cracked plate subjected to a remote tensile stress. Figure 2.3 schematically illustrates the effect of finite width on the crack tip stress distribution, which is represented by lines of force; the local stress is proportional to the spacing between lines of force. Since a tensile stress cannot be transmitted through a crack, the lines of force are diverted around the crack, resulting in a local

stress concentration (Anderson, 2005). The situation is comparable to running water in a river. A stone in the middle of the river obstructs the water and forces it around the stone at an increased velocity. In a very large river, the water will at some distance from the stone have the initial lower velocity since the obstacle is negligible compared to the width of the river. On the other hand, the same stone in a narrow river would cause the water to run at an increased velocity throughout the width of the river. The same applies for stresses in a cracked plate. In the infinite plate, the line of force at a distance *W* from the crack centerline has force components in the *x* and *y* directions. If the plate width is restricted to 2*W*, the *x* force must be zero on the free edge; this boundary condition causes the lines of force to be compressed, which results in higher stress intensification at the crack tip (Anderson, 2005).

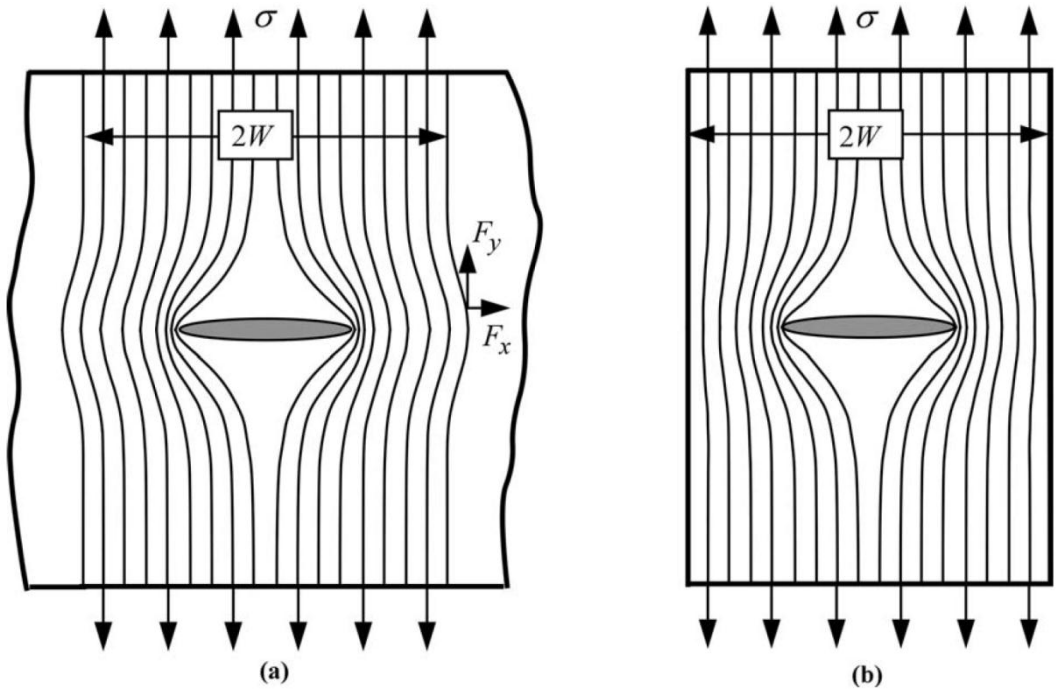

Figure 2.3: Stress concentration effects due to an elliptical crack in a finite and an infinite wide plate: (a) infinite plate, (b) finite plate (Anderson, 2005).

2.2 Energy release rate

When a system goes from a non-equilibrium state to equilibrium, there is conservation or a net decrease in energy. In 1920, Griffith applied this idea to the formation of a crack (Anderson, 2005). A crack can form only if such a process causes the total energy to decrease or remain constant. Thus the critical conditions for fracture can be defined as the point where crack growth occurs under equilibrium conditions, with no net change in total energy.

The Griffith energy balance for an incremental increase in the crack area dA, under equilibrium conditions, can be expressed in the following way:

$$\frac{dE}{dA} = \frac{d\Pi}{dA} + \frac{dW_s}{dA} = 0 \tag{2.1}$$

or

$$-\frac{d\Pi}{dA} = \frac{dW_s}{dA} \tag{2.2}$$

where E denotes total energy, W_s the work required to create new surfaces and Π the potential energy of an elastic body, which is defined as:

$$\Pi = U - F \tag{2.3}$$

where U is the strain energy stored in the body and F is work done by external forces.

In 1956, George R. Irwin proposed an elastic energy approach for fracture that is essentially equivalent to the Griffith model (Anderson, 2005). Irwin defined an *energy release rate* Γ, which is a measure of the energy available for an increment of crack extension:

$$\Gamma = -\frac{d\Pi}{dA} \tag{2.4}$$

The energy release rate, Γ, is the rate of change in potential energy with increase in crack area and is also referred to as the *crack driving force*. Crack extension occurs when the energy release rate reaches a critical value, Γ_c.

$$\Gamma_c = \frac{dW_s}{dA} \tag{2.5}$$

where Γ_c is a measure of the fracture toughness of the material. This is consistent with The Griffith energy balance in Equation (2.2).

The original concept by Griffith was partly developed by performing experimental tests on glass, and all of the potential energy released was thought to be used in the creation of the new surface on the crack faces. However, in more ductile materials, a majority of the energy may be used in deforming the material in the plastic zone at the crack tip, as illustrated in Figure 2.2. Irwin showed, by applying

Γ to metals, that the concept was applicable even under these circumstances if the plastic zone was small (*small scale yielding*) (Dowling, 2012).

The theory's dependence on a global linear elastic behaviour makes it a part of what is known as *linear-elastic fracture mechanics* (LEFM).

2.3 The stress intensity factor

The stress intensity factor, *K*, is used in fracture mechanics as a measure of the magnitude (intensity) of the stresses in the vicinity of an ideally sharp crack tip, or in other terms, the severity of a crack situation (Dowling, 2012). *K* is affected by the crack size, the objects geometry and applied stress. In defining *K*, one assumes linear-elastic material behaviour. The stress intensity factor is therefore also a part of the linear-elastic fracture mechanics.

A given material can resist a crack without fracturing as long as the stress intensity factor, *K*, is below a critical value, K_c, called the *fracture toughness*. Values of K_c vary a great deal for different materials and are affected by temperature, loading rate and secondarily the thickness of the member (Dowling, 2012). If the stress intensity at the crack tip of a loaded member reaches this critical value, the material is in an unstable state and brittle fracture may be expected.

Before we discuss the stress intensity factor any further, it is at this point important to present the different fracture modes defined in fracture mechanics.

2.3.1 Fracture modes

In fracture mechanics, a distinction is made between different modes of fracture propagation, depending on the loading situation. There are three different fractures modes. The stress intensity factor is usually given a subscript to denote the corresponding load and fracture mode (K_I, K_{II}, K_{III}).

Mode I, as shown in Figure 2.4, is caused from tensile stress normal to the plane of the crack. These tensile stresses are in the context of adhesive bonding referred to as peel stresses and are highly undesirable.

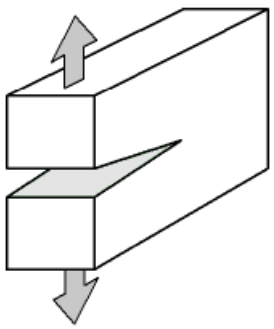

Figure 2.4: Mode I – Opening (eFunda, 2012)

Fracture Mode II, as shown in Figure 2.5, is caused from in-plane shear stress. This is the optimal fracture mode for bonded joints in terms of load capacity. It is therefore desirable to design the joints so they fracture in pure Mode II.

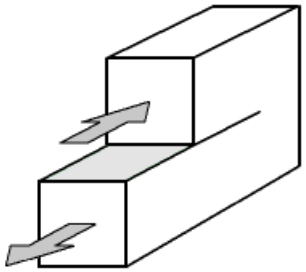

Figure 2.5: Mode II – In-Plane Shear (eFunda, 2012)

Fracture Mode III, as shown in Figure 2.6, is caused from out-of-plane shear stress.

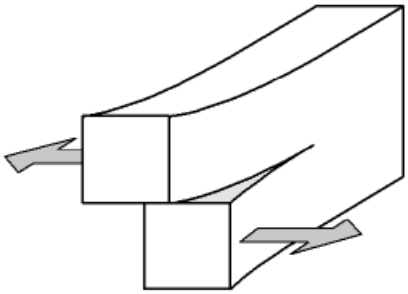

Figure 2.6: Mode III – Out-of-Plane Shear (eFunda, 2012)

Fractures can happen as a pure Mode I, Mode II or Mode III fracture or they can occur as a combination of fracture modes.

In the present thesis, stress intensity factors will only be discussed in relation with Mode I loading. As a convenience, the subscript on K_I will be dropped, and K without such a subscript is understood to denote K_I.

2.3.2 Solutions for determining the stress intensity

For an infinite wide centre cracked tensile plate (Mode I loaded) as illustrated in Figure 2.1, the stress intensity factor K only depends on the applied stress S, and the crack length a (measured from the centreline) and can be expressed as follows

$$K = S\sqrt{\pi a} \tag{2.2}$$

Equation (2.2) gives a good accuracy for geometries where the crack length is small compared to the plates width ($a << W$).

For different types of geometries it is in general convenient to express K as

$$K = FS\sqrt{\pi a} \tag{2.3}$$

where the factor F includes the effects of geometry, as finite width, and loading configurations. Solutions for F exist for a wide variety of configurations. Three of the most common, obtained from the "*The stress analysis of cracks handbook*" by Tada, Paris and Irwin, are listed below.

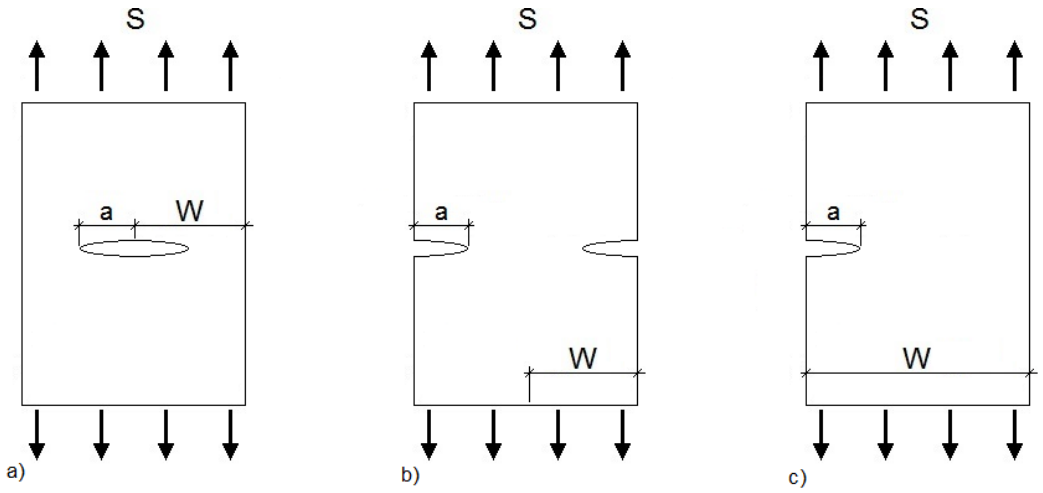

a) $$F = \frac{1 - 0.5\alpha + 0.326\alpha^2}{\sqrt{1-\alpha}} \tag{2.4}$$

b) $$F = \left(1 + 0.122\cos^4\frac{\pi\alpha}{2}\right)\sqrt{\frac{2}{\pi\alpha}\tan\frac{\pi\alpha}{2}} \tag{2.5}$$

c) $$F = 0.265(1-\alpha)^4 + \frac{0.857 + 0.265\alpha}{(1-\alpha)^{3/2}} \tag{2.6}$$

where $\alpha = \frac{a}{W}$

Figure 2.7: Stress intensity factors for three cases of cracked plates under tension (Tada, et al., 2000).

2.4 Relationship between K and Γ

Two key parameters in fracture mechanics have been introduced, the energy release rate and the stress intensity factor. The parameters represent the two main approaches to fracture analysis, the energy approach and the stress analysis approach.

The energy approach states that fracture occurs when the energy available for crack growth is sufficient to overcome the resistance of the material, and its key parameter, the energy release rate, quantifies the net change in potential energy that accompanies an increment of crack extension (Anderson, 2005). The resistance of the material, or its fracture toughness can be quantified by the critical energy release rate, Γ_c.

The stress intensity factor characterizes the magnitude of the stresses near the crack tip and the critical value of the stress intensity factor, K_c, is another measure of a material's fracture toughness.

The quantities of K and Γ for mode I fracture can be shown to be related as follows

$$\Gamma = \frac{K^2}{E'} \tag{2.6}$$

where E' is obtained from the material's young's modulus and Poisson's ratio ν:

$$\begin{aligned} E' &= E && \text{for plane stress} \\ E' &= \frac{E}{1-\nu^2} && \text{for plane strain} \end{aligned} \tag{2.7}$$

2.5 Fatigue crack growth

As mentioned earlier, the presence of cracks can significantly reduce the strength of structures. Even small flaws can by time develop and become a real threat to a structure. Under cyclic loading a small crack of an initially negligible size can grow until it reaches the critical size for brittle fracture, a_c, a behaviour called *fatigue crack growth*.

2.5.1 Fatigue crack growth rate

Consider a growing crack that increases by an amount Δa due to the application of a number of cycles ΔN. The rate of growth with cycles can be characterized by the ratio $\Delta a/\Delta N$ or, for small intervals, by the derivative da/dN. A value of the *fatigue crack growth rate* da/dN, is the slope at a point on an crack length versus cycles curve (Dowling, 2012).

The stress intensity factor *K*, can be used as a basis for fatigue crack growth analysis. As described in Section 0, the stress intensity factor defines the severity of a crack, and the rate of fatigue crack growth is therefore controlled by *K*.

K depends on the combination of crack length, geometry and loading, and can be expressed in the following manner:

$$K = FS\sqrt{\pi a} \tag{2.7}$$

For cyclic loading the stress intensity varies with the fluctuating nominal stresses. It is therefore necessary to look at the range of the stress intensity factor, Δ*K*. The stress intensity range is given by the difference between the maximum and minimum stress intensity of the load cycle, which is determined by the stress range Δ*S*. It is also convenient to introduce the stress ratio *R*.

$$\Delta S = S_{max} - S_{min}, \qquad R = \frac{S_{min}}{S_{max}} \tag{2.8}$$

$$\Delta K = F\Delta S\sqrt{\pi a} \tag{2.9}$$

The maximum and minimum value of *K* are given by

$$\begin{aligned} K_{max} &= FS_{max}\sqrt{\pi a} \\ K_{min} &= FS_{min}\sqrt{\pi a} \end{aligned} \tag{2.10}$$

The range of *K* can therefore be expressed as

$$\Delta K = K_{max} - K_{min} \tag{2.11}$$

Figure 2.8 is a schematic log-log plot of da/dN versus ΔK, which illustrates typical fatigue crack growth behavior in metals. The curve contains three distinct regions. At intermediate values of ΔK, the curve is linear (stage II). At low growth rates (stage I), the curve becomes steep and da/dN approaches zero at a threshold ΔK, the fatigue crack growth threshold, ΔK_{th}. Crack growth does not ordinarily occur below this limiting value of ΔK. At high values of ΔK, the growth rate may increase rapidly (stage III). This is due to rapid unstable crack growth just prior to final fracture.

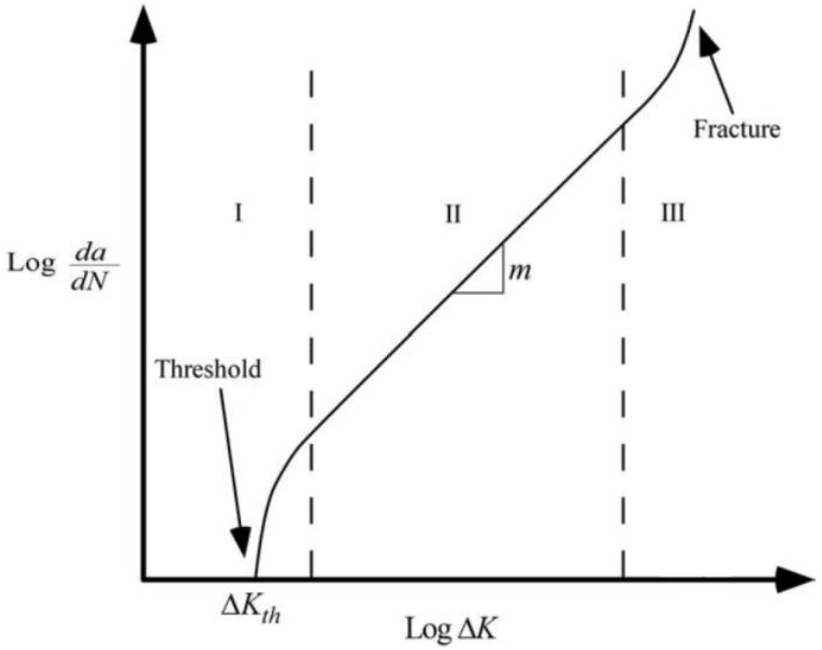

Figure 2.8: Typical fatigue crack growth behaviour in metal (Anderson, 2005).

The linear region of the plot in Figure 2.8 can be described by the following equation

$$\frac{da}{dN} = C(\Delta K)^m \tag{2.12}$$

where *C* and *m* are material constants that are determined experimentally. The equation has become known as the *Paris Law* after Paul Paris who first presented it in 1960 (Anderson, 2005).

The constants *C* and *m* for the intermediate region, where Equation (2.12) applies, have been suggested by Barsom for various classes of steel. These apply under zero-to-tension loading when $R \approx 0$ and are given in Table 2.1.

Table 2.1: Paris Law material constants for various classes of steel (Barsom & Stanley, 1999).

Class of steel	**C** $\left(\frac{mm/cycle}{(MPa\sqrt{m})^m}\right)$	**m**
Ferritic-pearlitic	$6.89 \cdot 10^{-9}$	3.0
Martensitic	$1.36 \cdot 10^{-7}$	2.25
Austenitic	$5.61 \cdot 10^{-9}$	3.25

While the stress intensity range is the main factor that governs the crack growth rate, the stress ratio *R*, also affects the rate. Generally, an increase in *R* results in an increase in *da/dN* for a given stress intensity range, ΔK, and vice versa.

2.5.2 Life estimates for constant amplitude loading

There is often a need to estimate the amount of cycles needed for a crack of an initial length, a_i, to grow to the critical length, a_f, where brittle fracture may occur. A common way to perform these life estimates is to make use of the Paris law for crack growth rate. However, since the crack growth rate *da/dN* depends on the stress intensity range ΔK, which increases with the crack length, the growth rate is not constant. The crack growth accelerates as the crack propagates. This situation of changing *da/dN* necessitates the use of an integration procedure to obtain the critical amount of cycles.

According to Paris the crack growth rate can be estimated with the following equation

$$\frac{da}{dN} = C(\Delta K)^m \tag{2.13}$$

where any effects of environment, frequency, etc., are assumed to be included in the material constants involved (Dowling, 2012). By solving Equation (2.13) for *dN* and integrating on both sides, we can calculate the cycles needed for a crack to grow from its initial length a_i, to a_f.

$$N_{if} = \int_{N_i}^{N_f} dN = \int_{a_i}^{a_f} \frac{1}{C(\Delta K)^m} da \tag{2.14}$$

From Section 2.5.1 we know that ΔK can be expressed in the following manner

$$\Delta K = F\Delta S\sqrt{\pi a} \tag{2.15}$$

If the stress range ΔS is constant and the factor *F* can be approximated as constant over the length a_{if}, the number of cycles can be expressed as follows

$$N_{if} = \int_{a_i}^{a_f} \frac{1}{C\left(F\Delta S\sqrt{\pi}\right)^m} da = \int_{a_i}^{a_f} \frac{1}{C\left(F\Delta S\sqrt{\pi}\right)^m} \frac{da}{a^{m/2}} \tag{2.16}$$

Integration of Equation ((2.16) gives the following simple expression for the number of cycles, N_{if}:

$$N_{if} = \frac{a_f^{1-m/2} - a_i^{1-m/2}}{C\left(F\Delta S\sqrt{\pi}\right)^m \left(1 - \frac{m}{2}\right)} \tag{2.17}$$

Since the crack growth rate increases as a crack propagates, more cycles are needed to increase a growing crack by an amount Δa near the initial crack length a_i, then it is at a later stage closer to a_f. Hence, most of the cycles calculated by a solution for N_{if} are accumulated near a_i. Consequently, for situations where a_f is substantially larger than a_i, Equation (2.17) is insensitive to the value of a_f. The value of a constant F should therefore be closer to the value F_i (corresponding to a_i), than the value F_f (corresponding to a_f). According to Dowling it is wise to either use F_i or a slightly higher intermediate value (Dowling, 2012).

Crack growth life estimates by Equation (2.17) require that the factor F can be approximated as constant. For situations where F_i and F_f differ to such an extent that F must be treated as a variable, numerical integration is usually needed. If F_i and F_f differ by more than about 15 to 20 %, the resulting error in N_{if} due to using a constant value of F will generally be unacceptably large (Dowling, 2012).

2.5.3 Critical crack length

As a crack propagates under constant cyclic loading, the value of K_{max} increases until it reaches the material fracture toughness K_c. At this point the stress intensity at the crack tip is so severe that a full failure is expected. The corresponding crack length a_c can be calculated with Equation (2.18). Since F varies with the crack length, a graphical or iterative solution is generally needed.

$$a_c = \frac{1}{\pi}\left(\frac{K_{IC}}{FS_{max}}\right)^2 \tag{2.18}$$

Although a_c is the critical crack length in terms of stress intensity, fracture may occur at a shorter crack length due to plastic yielding. Because of loss of cross-sectional area, the stress in the remaining cross-section may increase to the yielding strength of the material before the stress intensity reaches K_{Ic}. The corresponding crack length to fully plastic yielding may be referred to as a_y. The smaller of the two, a_c and a_y, should be chosen as a_f.

2.6 Limitations of LEFM

In Section 2.1, it was noted that actual materials cannot support the theoretically infinite stresses at the tip of a sharp crack, so that upon loading, a region of yielding forms and the crack tip becomes blunted. An important restriction to the use of LEFM is that the size if this plastic zone at the crack tip must be small relative to the crack length as well as the geometrical dimensions of the specimen or

part. Otherwise, a plasticity correction is required for the stress intensity factor, *K*, or elastic-plastic fracture mechanics (EPFM) may be needed.

If the plastic zone is sufficiently small, there will be a region outside of it, the *K-field*, where the elastic theory still applies. The *K*-field surrounds and controls the behaviour of the plastic zone and the crack tip area. Thus, the stress intensity factor continues to characterize the severity of the crack situation, despite the occurrence of some plastic deformation (Dowling, 2012). If the plastic zone, however, is so large that it eliminates the *K-field*, the liner-elastic fracture mechanics no longer apply.

Dowling (Dowling, 2012) presents an overall limit on the use of LEFM, where LEFM is valid if

$$a, (W - a), h \geq \frac{4}{\pi}\left(\frac{K}{\sigma_{ys}}\right)^2 \tag{2.19}$$

The right side of Equation (2.19) equals a distance of four times the diameter of the plastic zone in a plain stress situation. The distances *a*, (*W* – *a*) and *h* are presented in Figure 2.9.

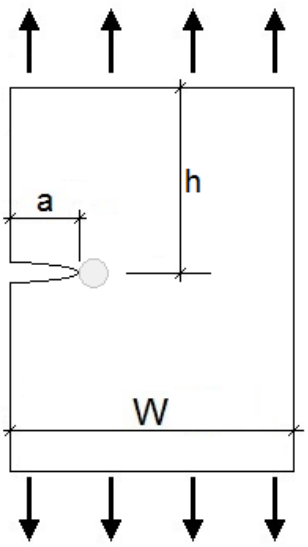

Figure 2.9: A crack and its plastic zone with relevant dimensions.

Chapter 3

Adhesively bonded Joints

The present chapter contains a brief introduction to adhesively bonded joints and relevant theory. First, bonded joints that are commonly found in engineering practice will be presented. Then, the difference between short and long overlap lengths in bonded joints will be illustrated and discussed. Thereafter, various methods of failure analyses will be briefly introduced.

3.1 Bonded joint configurations

Adhesively bonded joints exist in a variety of shapes and forms. Figure 3.1 - Figure 3.5 illustrates some of the most common.

Figure 3.1: Single butt strap (with composite overlap)

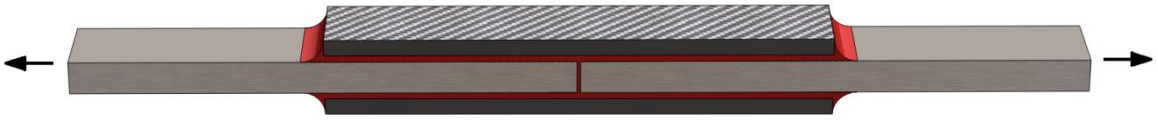

Figure 3.2: Double butt strap (with composite overlap)

Figure 3.3: Single lap

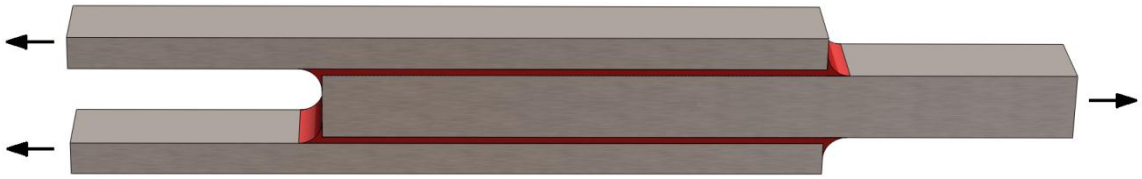

Figure 3.4: Double lap

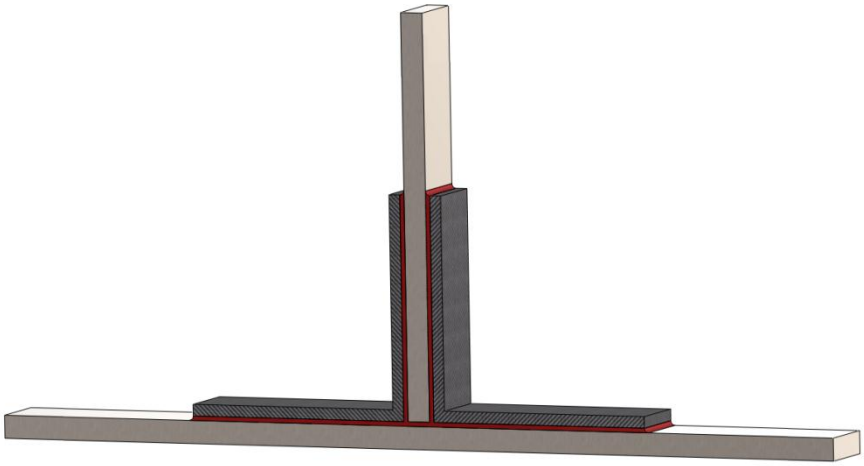

Figure 3.5: T-joint

In the present thesis, the main emphasis will be on the double butt strap (DBS) joint. A DBS joint, consist of two substrates bonded together with an adhesive and a set of plates/patches that overlap the joint. The structural members of the joint (the substrates and overlaps), are referred to as the adherends (Adams, et al., 1997).

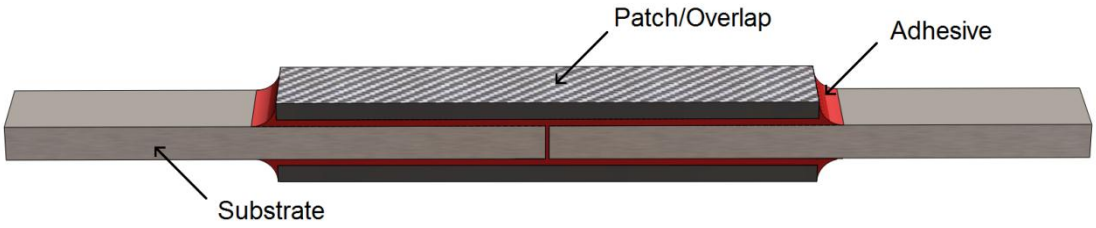

Figure 3.6: Double butt strap joint

An advantage with the DBS joint is the symmetrical properties, which eliminate bending moments and makes it easier to model in finite element software. With a single lap (SL) joint, such as the one

in Figure 3.3, the loads are not collinear. And a bending moment must therefore exist and the joint will rotate as shown in Figure 3.7.

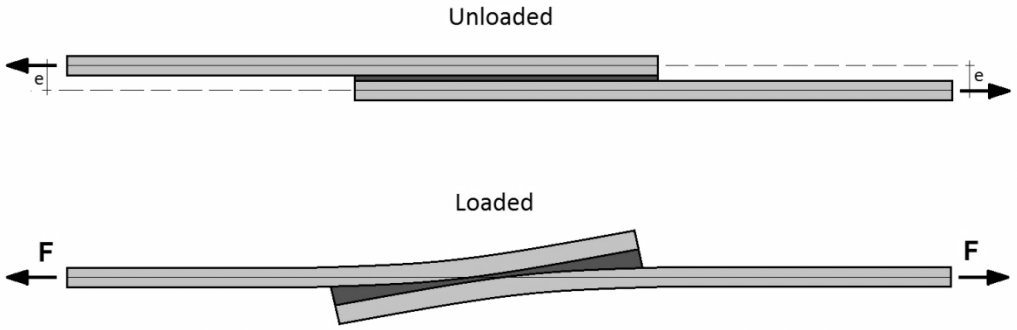

Figure 3.7: Deformed single lap joint

While the adherends of the DBS joint are loaded solely in tension, the adherends of the SL joint are experiencing a bending moment. This generates a more complex stress state, and the adhesive is facing peel stresses at the ends of the joint. Peel, as Adams puts it, *"is the hated enemy of the joint designer"* (Adams, et al., 1997). These stresses can lead to reduced load-capacity and should therefore be avoided.

Although there is no net bending moment in the DBS joint, it is experiencing internal bending moments as shown in Figure 3.8.

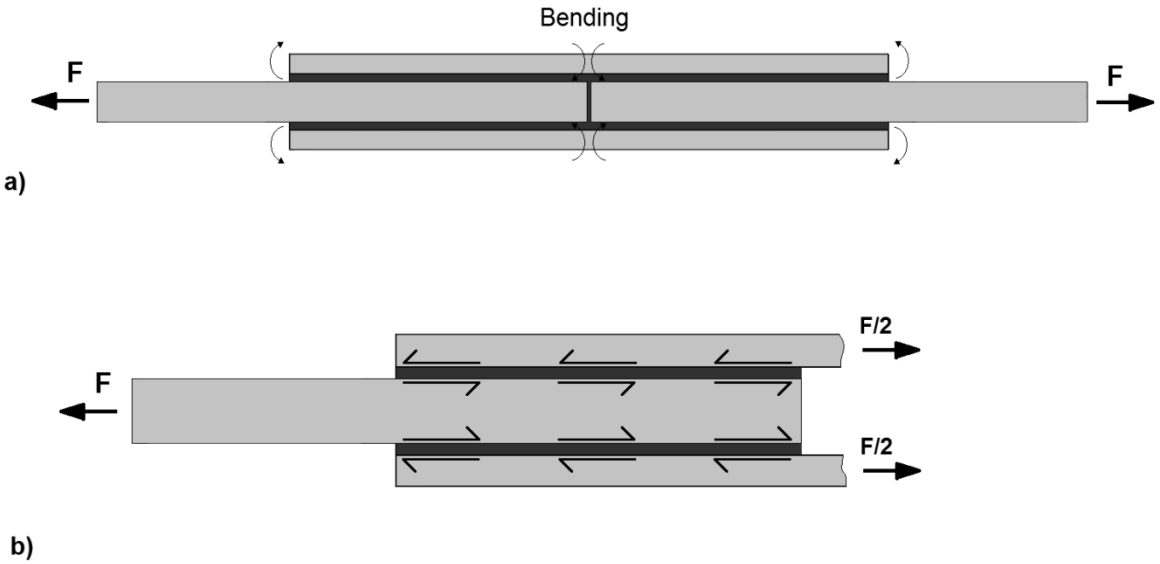

Figure 3.8: Internal moments in a DBS joint. a) Complete joint. b) Left half of the joint.

The outer adherends bend, giving rise to tensile stresses in the adhesive layer at the ends of the overlaps and compressive stresses in the joint centre.

3.2 Overlap length

A joint with a short overlap shows a fundamentally different kind of behaviour than a joint with long overlap. McGeorge has explained this in a simple manner in *Engineering Fracture Mechanics* (McGeorge, 2010), and the key points of his article are presented in this chapter.

To understand the mechanical behaviour of an adhesively bonded joint and the effects of short and long overlap, it is useful to take a closer look at a simple single butt strap (SBS) joint as illustrated in Figure 3.9.

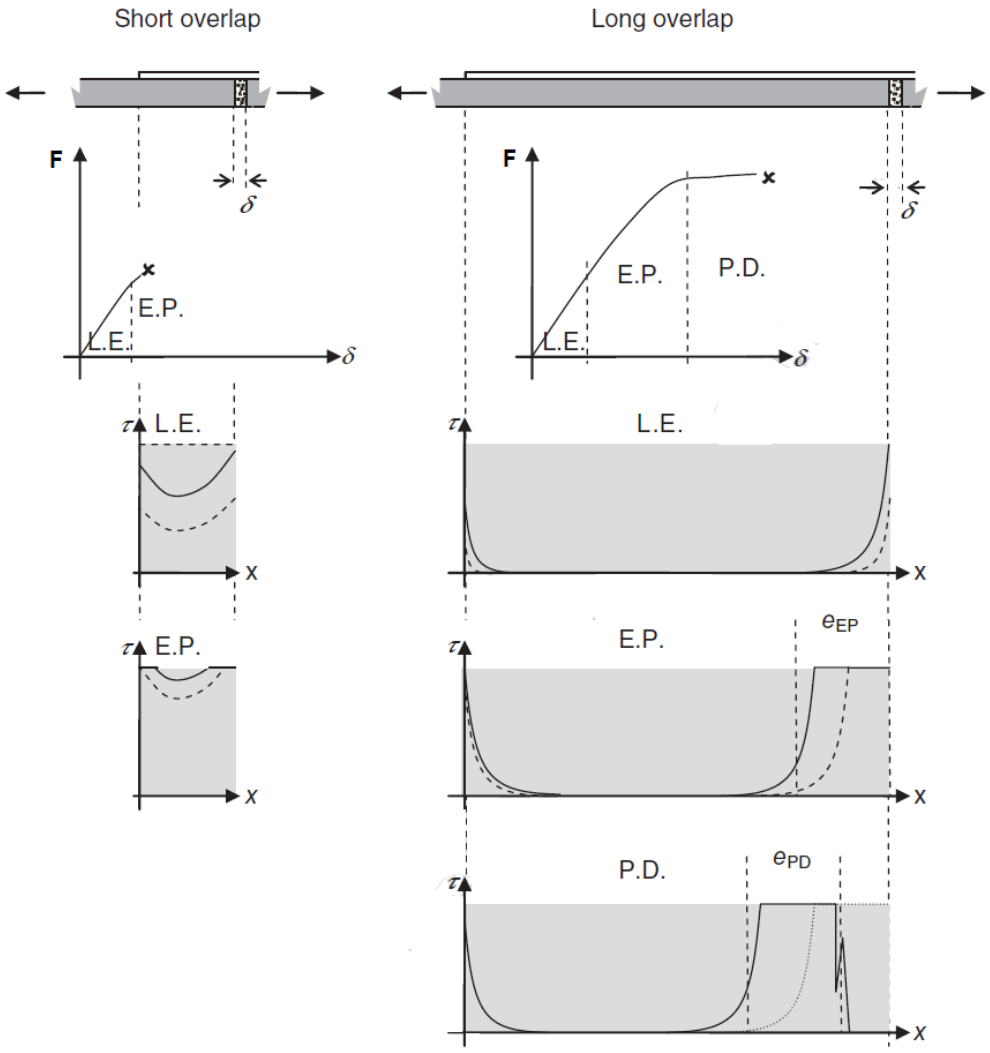

Figure 3.9: Mechanical response of bonded joint with short and long overlap (McGeorge, 2012)

Figure 3.9 shows a SBS joint with short and long overlap loaded with a tensile force, *F*. The diagrams show the applied force (*F*) as a function of the relative displacement between the inner adherends,δ, and typical distributions of shear stress (τ) along the bondline at various levels of applied loading.

It is assumed that the behaviour of the adhesive material can be considered to be linearly elastic when the stress is below yield stress, and then perfectly plastic thereafter as illustrated in Figure 3.10.

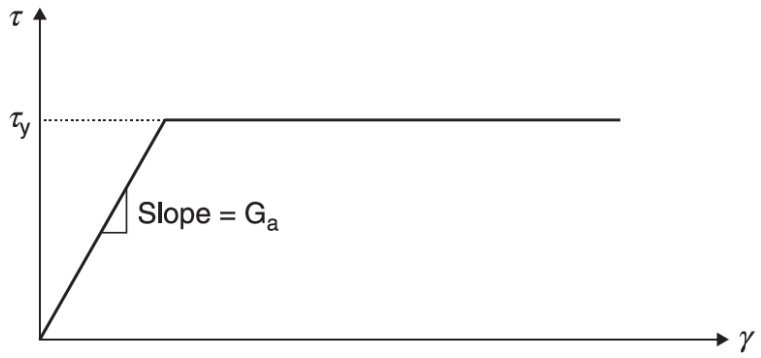

Figure 3.10: Ideal elastic-plastic material behaviour

For simplicity, consider an unbalanced joint where the in-plane stiffness of the overlap is lower than that of the inner adherends. With a short overlap (as shown on the left side of Figure 3.9), the response of the bondline is linear elastic (denoted L.E.) at a low load. When the stress reaches the critical shear stress at the right end of the overlap, the material begins to deform plastically at that end. As the applied load is gradually increased, the length of the zone that has reached a plastic state grows whereas the behaviour of the rest of the bondline remains elastic. The bondline's response is now elastic-plastic, denoted E.P. in the figure. As the loading increases the plastic area of the bondline grows until the bondline is fully plastic, and fracture is a fact. The joint has reached its maximum capacity when the whole bondline has reached yield stress and is then unable to transmit a higher load. Thus, for short overlap lengths the capacity is proportional to the length of the overlap.

Now let's take a look at the long overlap on the right side of Figure 3.9. As with the short overlap the response is linear-elastic at low loading. In this loading range, the bondline shear stresses are located at the ends of the overlap leaving the central parts of the bondline nearly unloaded. As the maximum shear stress at the right end reaches the yield stress, a plastic zone develops there. The length of this plastic zone increases with increasing loading. Note that as long as the plastic zone grows, the *F*-δ curve will continue to rise. Furthermore, due to the elastic zone that remains in the centre of the bondline, the relative displacement between the adherends will be dominated by the elastic stresses and thus be almost linear. Although the stress at the right end does not increase, the local strain keeps on growing until critical strain is reached. At this point fracture will develop at that end. The magnitude of δ at the maximum loading provides an estimate of the critical strain in that particular case. The critical strain is not a property of the adhesive but is simply the inelastic strain that happens to have been reached when fracture occurs. At this point the plastic zone has grown to a certain length (e_{PD}), and under a stable fracture the bondline will fracture from the right side and

move towards the other end under constant loading. As this happens the plastic zone will be "pushed" leftwards in the adhesive bondline. Thus, as long as the overlap is sufficiently long, strength of bonded joints is independent of overlap length.

3.3 Failure predictions of adhesively bonded joints

We will now take a look at different approaches for analysing the strength of adhesively bonded joints.

When predicting the static capacity of bonded joints there are basically two challenges one needs to overcome. Firstly, there is a need to model the response of the joint to the applied forces in terms of stresses, strains and deformations. Secondly, the model must be able to predict, based on the joint response to the applied forces, at what load level failure will occur (McGeorge, 2012).

Two different categories have been proposed for failure predictions. Traditionally the capacity of adhesive joints has been analysed using the "strength of materials approach". This approach is based on the assumption that fracture of the bondline will occur when the adhesive reaches a critical stress or strain level. A more recent approach is based on the theory of fracture mechanics. It observes that failure occurs by fracture and hence balances the energy available to drive a fracture to some fracture resistance of the material. This approach can be referred to as the "fracture mechanics approach" (McGeorge, 2012).

3.3.1 Elastic strength of materials models

In elastic strength of material approaches, one assumes linear elastic behaviour of the adhesives and adherends. A much used method is the critical stress approach. The approach assumes that fracture will occur when the bondline reaches a critical stress level. The critical stress level is obtained by analysing a joint that has been tested to failure. The maximum value of the bondline shear stress at failure is then selected as the critical stress. The basic idea of the method is that this critical stress level can be applied as a failure criterion for a wide range of joints with the same type of adhesive.

There are several elastic theories available for the material response analysis. All these models, however, predict that the stresses in the bondline depend on the bondline thickness, and that the stresses decrease with increasing bondline thickness, which is contrary to experimental evidence (McGeorge, 2012). It is also known that a part of the bondline will reach yield stress before the joint fractures, thus models aiming at predicting the failure load of bonded joints should account for inelastic material behaviour.

3.3.2 Inelastic strength of materials models

The natural extension to the critical stress approach is to allow for nonlinear material behaviour in the adhesive bondline. This will allow loading to be increased beyond the linear elastic failure load prediction.

With plasticity taken into account, the stress predicted at failure will always equal the yield stress. Thus a critical stress level cannot be used as a failure criterion for inelastic strength of materials models. In 1973, Hart-Smith developed a method including adhesive plasticity (Hart-Smith, 1973). The method was based on the principle that bonded joints would fail when a certain critical plastic strain level is reached in the bondline. Experiments show, however, that strain at failure is not a material constant and that critical strain based models fail to give reliable predictions of the strength of bonded joints (McGeorge, 2010). As with the critical stress approach, joint capacity predicted with the critical plastic strain also depends on the bondline thickness, which is contrary to experimental evidence.

3.3.3 Inelastic fracture mechanics approach

The failure of the strength of materials approaches to represent the observed behaviour of bonded joints motivated the development of a new model built on fracture mechanics theory. The model, developed by McGeorge, is based on the energy approach developed by Griffith and Irwin that was presented in Section 0. McGeorge has adapted the approach to include inelastic material behaviour. Thus the dissipation of energy due to plastic deformation is also taken into account.

The basic assumption of this approach is that final fracture of the bondline occurs at the applied loading where the energy available to progress the damage exceeds the damage resistance of the bondline. There are four distinct contributions to the energy balance:

1. The work performed by the externally applied forces
2. The elastic energy released from the specimen
3. The work dissipated due to plastic deformations in the bondline
4. The work of creating the damage to the adhesive bondline.

To proceed with this approach, it is necessary to establish the distribution of stresses and strains in the adherends and bondline that is reasonably representative of what occurs when the joint is loaded up to its capacity. For simple joint geometries and with a few simplifying assumptions, it is possible to establish simple formulae for the stresses and strains. The assumptions are:

- Long overlap length, implying zero adhesive shear stress in the central part of the bondline.
- Damaged material is considered unable to transfer any significant shear stress.
- The adhesive is assumed to have an ideal plastic behaviour.
- No rotations of the substrates.

With these assumptions, McGeorge was able to derive simple formulae for the elastic energy in the adherends and adhesive as well as for the inelastic dissipation of energy in the bondline. Those formulae could again be used to derive a simple equation for the energy release rate (Γ) occurring at the most highly loaded end of the bondline of an unbalanced single butt strap joint with long overlap. The SBS joint is assumed to be restricted from rotation as illustrated in Figure 3.11.

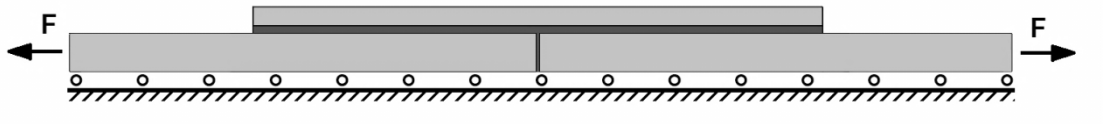

Figure 3.11: Single butt strap joint restricted from rotating.

The simple equation for the energy release rate at fracture loading is expressed as:

$$\Gamma_c = \frac{{F_{max}}^2(E_s t_s + 3E_0 t_0)}{3E_0 t_0 w^2 (E_s t_s + E_0 t_0)} \tag{3.1}$$

Rewriting Equation (3.1) gives us the predicted joint failure load, F_{max}:

$$F_{max} = w\sqrt{\frac{3E_0 t_0 \Gamma_c (E_s t_s + E_0 t_0)}{E_s t_s + 3E_0 t_0}} \tag{3.2}$$

where *E* denotes Young's Modulus and *t* the plate thickness. Subscript *o* denotes the overlap and subscript *s* denotes the substrate.

From Equation (3.2) we can see that:

- The predicted joint capacity is independent of the bondline thickness.
- The predicted joint capacity depends on the stiffness of the overlap and the adherends and the critical energy release rate.
- The predicted joint capacity does not depend on of the shear stiffness, shear modulus or the shear yield stress of the adhesive.
- The predicted joint capacity does not depend on a critical shear strain in the adhesive.

3.3.4 Inelastic fracture mechanics approach – Cohesive FE analysis

In the process of deriving the simple equation for the critical energy release rate, Equation (3.1), McGeorge made several simplifying assumptions. This analytical approach is also limited to problems with simple geometry. However, with the use of finite element software these simplifying assumptions are no longer needed and one can model joints with a wide range of geometry.

When simulating bonded joints with finite element software the adhesive bondline can be modelled using cohesive elements. Cohesive elements have the ability to simulate failure based on a pre-described fracture toughness.

McGeorge compared his analytical approach with test results from actual joints tested to failure. The results indicated that the critical energy release rate is a property of the adhesive bondline, the fracture toughness, independent of bondline thickness and joint configuration. With the help of finite element software and the use of cohesive elements, a student at the University of Oslo was able to test this theory (Osnes & Guthu, 2011).

Three joints with long overlap were modelled with cohesive elements. These models were then used to simulate fracture in the adhesive bondline. To start, the failure load of a joint with a 3 mm CFRP (Carbon Fibre Reinforced Polyester laminate) overlap was used for calibration. The load was assumed to be 71,2 kN for long overlap lengths and the fracture toughness was determined to be 4700 J/m^2. This fracture toughness was then used for all the joints in the FE analysis.

By using Equation (3.1) the critical energy release rate was determined to be 4730 J/m^2 for the same joint. This energy release rate was then used as the fracture toughness in the analytical formula for all of the three joints.

In Table 3.1, the analytical strength predictions are compared with results from the finite element analyses and experiments. As one can see they are showing very good agreement.

Table 3.1: Observed failure loads compared with theoretical predictions using the analytical and finite element fracture based approaches

	Experimental failure loads (kN)	**Fracture toughness used in the FE models (J/m^2)**	**Predicted failure loads from the FE models (kN)**	**Fracture toughness used in the analytical formula (J/m^2)**	**Predicted failure loads from the analytical formula (kN)**
3 mm CFRP joint	71,2	4700	71,2	4730	71,2
5 mm GFRP joint	45,1	4700	42,2	4730	47,0
6 mm GFRE joint	47,6	4700	46,2	4730	50,9

Chapter 4

Finite element analysis of SENT steel plate with CFRP reinforcement

This chapter contains a detailed description of the modelling of a single-edge notched tension (SENT) steel plate with double CFRP reinforcement. The plate is modelled in the commercial finite element software, Abaqus. The main objective of the modelling is to examine the effects of the CFRP patches, and study their ability to reduce the stress intensity at the crack tip.

In order to get reliable results from the FE model is it essential that the adhesive layers are simulated in a satisfying manner. To make sure that the material properties of the adhesive were correct, an existing well-functioning two-dimensional model of a DBS joint with CFRP overlaps was remodelled in three-dimensions and then adapted in to the double reinforced SENT plate.

4.1 DBS joint

As mentioned in Section 3.3.4, a student at the University of Oslo, Geir O. Guthu, has recently performed studies that have resulted in a promising model for strength predictions of adhesively bonded joints (Guthu, 2010). Guthu produced a model of a double butt strap joint with steel substrates and composite overlaps. The adhesive layers of the model were represented by cohesive elements in order to simulate fracture. The model displayed good agreement with existing test results and analytical solutions, both in terms of general material behaviour and predicted fracture loads. In a project prior to the present MSc project, Guthu's work has been studied in detail and his model has successfully been remodelled in Abaqus (Rotwitt, 2012). In the present thesis, this two-dimensional model has been reproduced in three-dimensions and modified to a single-edge notched tension steel plate.

An overview of the reproduction of the DBS joint model will be presented in this chapter. The use of cohesive elements involves a rather comprehensive modelling process, but the description in this section is kept to a minimum. The full extent of the modelling can be studied in Guthu's "Modelling of Mechanical Response and Fracture in Adhesively Bonded Joints" (Guthu, 2010).

Prior to describing the modelling process, it is appropriate to present a short introduction to the use of cohesive elements in Abaqus.

4.1.1 Cohesive elements

Abaqus offers a library of cohesive elements to model the behaviour of adhesive joints, interfaces in composites, and other situations where the integrity and strength of interfaces may be of interest.

These elements can be used to model finite-thickness adhesives and they have the property that a failure criterion can be used to determine when the elements fail, and one of the optional failure criteria is the critical energy release rate.

The elements are placed where a crack is expected to propagate, but the model does not need to have any crack to begin with. The precise locations (among the areas modelled with cohesive elements) where cracks initiate, as well as the evolution characteristics of such cracks, are determined as part of the solution (Dassault systèmes, 2012).

Cohesive elements can be used to model all the three fracture modes described in Chapter 2.3.1. However, the main goal is to predict pure mode II fracture in the bondline of the DBS joint. The cohesive elements used in the FE model will therefore primarily be developed for pure mode II fracture.

The cohesive elements in the present thesis are based on a traction-separation law. The available traction-separation model in Abaqus assumes initially linear elastic behaviour followed by the initiation and evolution of damage. The elastic behaviour is written in terms of an elastic constitutive matrix that relates the nominal stresses to the nominal strains across the interface. The nominal stresses are the force components divided by the original area at each integration point, while the nominal strains are the separations divided by the original thickness at each integration point. The default value of the original thickness is 1.0 which ensures that the nominal strain is equal to the separation (i.e., relative displacements of the top and bottom faces). The constitutive thickness used for traction-separation response is independent of the geometric thickness which in our case is 0.5 (Dassault systèmes, 2012).

The cohesive elements have a nominal traction stress vector, $\boldsymbol{s}$, consisting of three components in three-dimensional problems: s_n, s_s and s_t, which represent the normal and the two shear tractions. The corresponding separations are denoted by δ_n, δ_s and δ_t. The nominal strains can be defined as:

$$\varepsilon_n = \frac{\delta_n}{T_o}, \qquad \varepsilon_s = \frac{\delta_s}{T_o}, \qquad \varepsilon_t = \frac{\delta_t}{T_o}$$

Since the original thickness of the cohesive element, T_o, is equal to 1 as default in Abaqus, the nominal strains are equal to the separations.

$$\varepsilon_n = \delta_n, \qquad \varepsilon_s = \delta_s, \qquad \varepsilon_t = \delta_t$$

The elastic behaviour of the elements can then be written as:

$$\boldsymbol{s} = \begin{Bmatrix} S_n \\ S_s \\ S_t \end{Bmatrix} = \begin{bmatrix} K_{nn} & K_{ns} & K_{nt} \\ K_{sn} & K_{ss} & K_{st} \\ K_{tn} & K_{ts} & K_{tt} \end{bmatrix} \begin{Bmatrix} \varepsilon_n \\ \varepsilon_s \\ \varepsilon_t \end{Bmatrix} = \boldsymbol{K\varepsilon}$$

Damage modelling

Each failure mechanism consists of three ingredients: a damage initiation criterion, a damage evolution law, and a choice of element removal (or deletion) upon reaching a completely damaged state.

The initial response of the cohesive element is assumed to be linear as discussed above, but once a damage initiation criterion is met, material damage occurs according to a user-defined damage evolution law.

Figure 4.1 shows a typical traction-separation response with a failure mechanism.

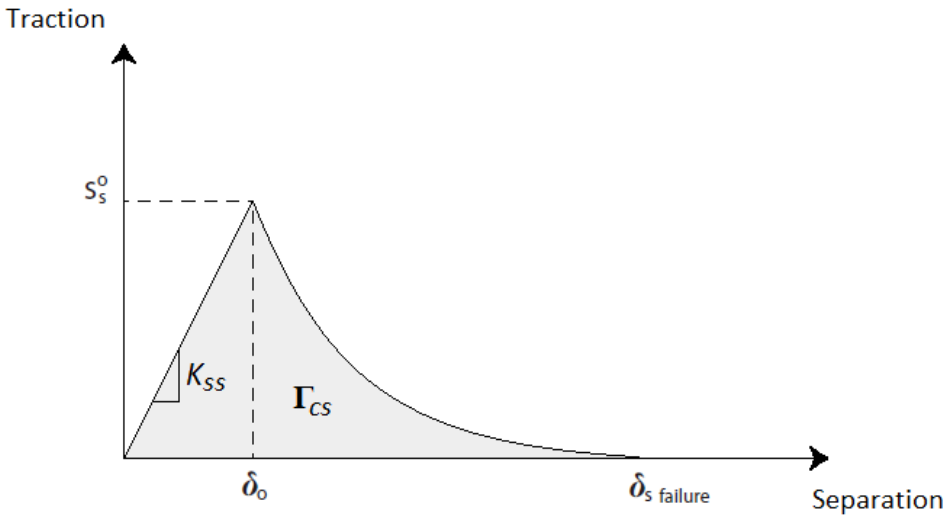

Figure 4.1: Traction-separation response for mode 2 failure with exponential softening

As we can see from the figure, the response of the elements are initially linear elastic until damage is initiated when the stresses and/or strains reaches a certain damage initiation criterion. In our case the damage initiation criterion is the critical stress level, s_s^o. When the critical stress level is reached the elements degrade according to the damage evolution law. The damage evolution law describes the rate at which the material stiffness is degraded until fracture. After fracture the elements are removed from the model. The shaded area under the traction-separation curve is the critical energy release rate for mode II fracture, Γ_{cs}.

Each failure mode has a traction-separation curve like the one above, and all consist of three ingredients: element stiffness (K), a damage initiation criterion (s^o) and a damage evolution law (Γ_c).

In a three-dimensional plain strain FE model, cohesive elements need nine input variables to describe the wanted traction-separation curve; they are as follows:

- s_n^o, which is the nominal tensile damage initiation traction for mode I fracture.
- s_s^o, which is the nominal shear damage initiation traction for mode II fracture.

- s_t^o, which is the nominal shear damage initiation traction for mode III fracture.
- K_{nn}, which is the elastic tensile stiffness for mode I fracture.
- K_{ss}, which is the elastic shear stiffness for mode II fracture.
- K_{tt}, which is the elastic shear stiffness for mode III fracture.
- Γ_{cn}, which is the critical energy release rate for mode I fracture.
- Γ_{cs}, which is the critical energy release rate for mode II fracture.
- Γ_{ct}, which is the critical energy release rate for mode III fracture.

4.1.2 Model Geometry

Guthu calibrated and tested his model against experimental results from a project of the MARSTRUCT Research Network of Excellence on marine structures (Hashim, et al., 2009). The geometry chosen for his models were therefore the same as for the test specimens of the project. The specimens were DBS joints with a range of overlap materials and lengths.

The specimen that has been reproduced in this thesis has 3 mm thick and 200 mm long CFRP overlaps. The geometry is illustrated in Figure 4.2.

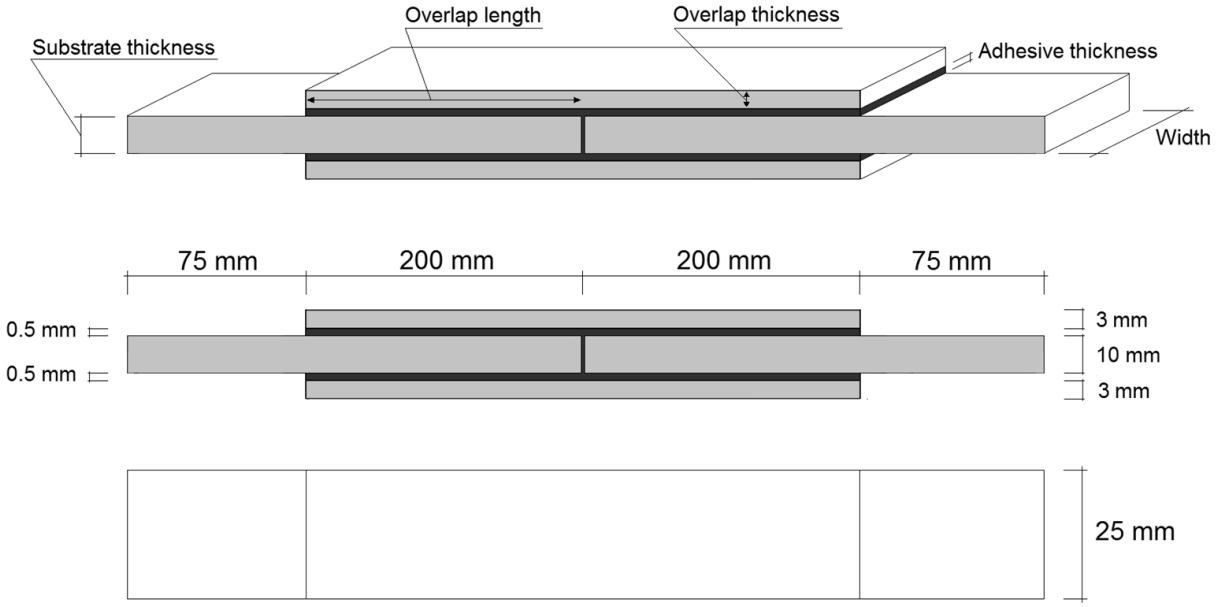

Figure 4.2: Specimen geometry

Due to the symmetry of the DBS joint, the model could be reduced to just a quarter of its original size, hence easing the modelling process and reducing calculation time.

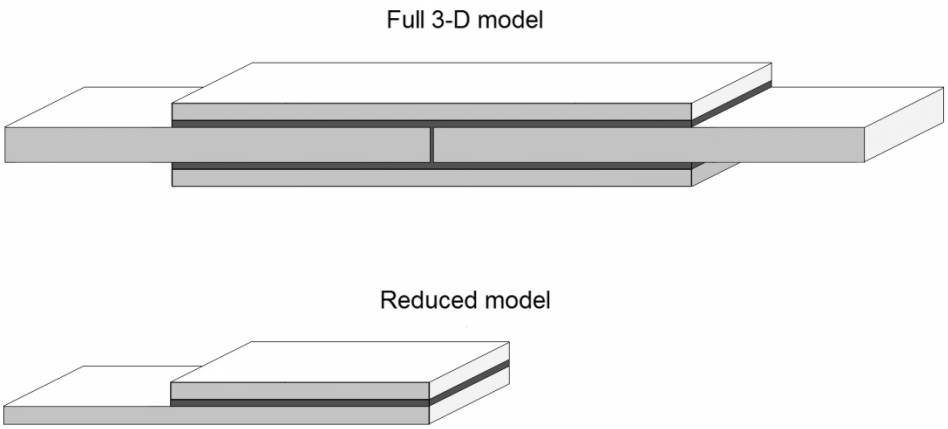

Figure 4.3: Reduction of the model size

The model now consists of three different parts, the steel substrate, overlap and the adhesive layer. Each part of the assembly is assigned its own section, material properties, and element mesh.

4.1.3 Element type

The steel substrates and the composite overlays are modelled with C3D20R elements. These are solid quadratic twenty node elements with reduced integration. The elements have three displacement degrees of freedom in each node.

The adhesive layer is, as described in Section 4.1.1, modelled with cohesive elements.

4.1.4 Constraints

To make the assembly of the three parts, one has to apply some constraints or contact conditions to the model. There are in Abaqus several ways to do this, but the method of choice for models with adhesives seems to be a surface-to-surface constraint named Tie. Surface-to-surface contact interactions can describe contact between two deformable surfaces and make the translational degrees of freedom equal for the two surfaces. The tie-constraint approach also allows the user to model the adhesive layer using a finer discretization than that of the substrate and the overlap.

Figure 4.4 illustrates the connecting surfaces. To be able to define a surface on the substrate that corresponded with the overlap length, the substrate had to be sectioned in to two parts.

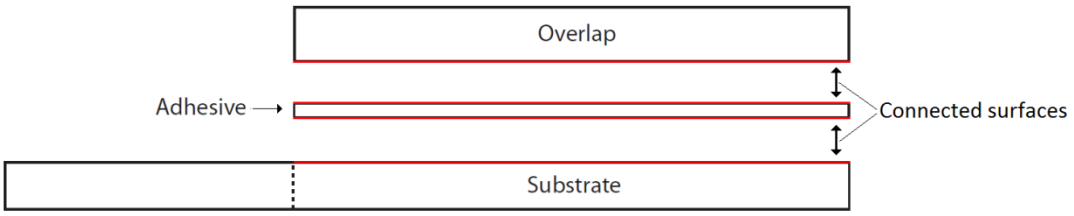

Figure 4.4: Surface-to-surface constraints

4.1.5 Boundary Conditions

In addition to the constraints between the different parts of the assembly one also has to impose some boundary conditions to the model. These boundary conditions must simulate the surrounding parts of the joint that was removed while reducing the size of the model.

The boundary conditions applied in the model is illustrated below.

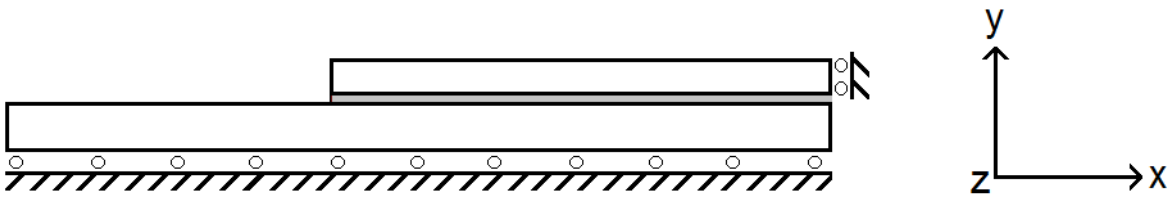

Figure 4.5: Boundary conditions

Symmetry boundary conditions about the y-plane are assigned to the steel substrate's bottom surface. This restrains the substrate from moving in the vertical direction and rotating around the x- and z-axes. The support allows movement in the horizontal direction.

The overlap's right side are assigned symmetry boundary conditions about the x-plane. This restrains the surface from movement in the x-direction and from rotating around the y- and z-axes.

The right surface of the substrate is not restrained in any way since the two substrates already is separated at this point. Nor is the adhesive restrained at this point since a crack will propagate at the centre of the joint at low loads.

The imposed restraints on the rotational degrees of freedom have no effect as the chosen elements only have displacement degrees of freedom. This is consistent for all FE models throughout the thesis.

4.1.6 Loading

Loading in Abaqus may be applied in three different ways: displacement control, pressure control and force control on a node set. The method of loading chosen for the analyses presented in this thesis was the pressure control. With pressure control a uniform negative pressure can be applied on the left surface of the steel substrate. For each step in an analysis a "Load Proportionality Factor" (LPF) is visible. The LPF shows the share of the defined pressure that is applied at each step. The actual applied force at a particular step is calculated by multiplying the LPF for the given step with the defined pressure and the cross-sectional area of the substrate. Since the substrate was cut in half when the size of the model was being reduced, the load also needs to be multiplied by two.

4.1.7 Material Properties

In this section material properties for the different parts will be presented. To be able to compare the results from the FE-model with the results from the test specimens the material properties are chosen to be same as for those materials that were tested.

Substrate

The tests were performed using steel substrates. The isotropic material properties for the steel are presented in Table 4.1.

Table 4.1: Material properties for steel substrates

	Steel
Young's modulus [GPa]	206
Poisson's ratio	0.3
Tensile strength [MPa]	395

Overlap

The DBS joints were tested with several different types of overlap materials. The specimen chosen for this thesis has a CFRP overlap. The mechanical properties for the overlap are presented in Table 4.2.

Table 4.2: Mechanical properties of the overlap materials

	CFRP
Longitudinal elastic modulus [GPa] [E_1]	62
Transverse elastic modulus [GPa] [E_2]	5.5
Transverse shear modulus [GPa] [G_{12}]	3.3
Poisson's ratio [ν_{12}]	0.3

Adhesive

The adhesive used in the experimentally tested joints was Araldite 2015. The adhesive's isotropic material properties are presented in Table 4.3.

Table 4.3: Material properties for the adhesive

	Araldite 2015
Young's modulus [GPa]	1.8
Poisson's ratio	0.36
Shear yield stress, τ_y [MPa]	20

The adhesive layer is modelled with cohesive elements so the nine input variables, presented in Section 4.1.1, that define the behaviour of the elements must be found.

Elastic stiffness of the elements

First, we are defining the elastic stiffness of the elements, K_{nn}, K_{ss} and K_{tt}. This is done by calibrating the cohesive FE-model with a model where the adhesive layer is represented by solid elements. To do this a path was created between the adhesive layer and the overlap in the two models. This path makes it possible to plot the stress and strain distribution along the joint bondline. Comparisons of plots of the stress distribution in the two models, with and without cohesive elements, resulted in the element properties presented in Table 4.4

Damage initiation criteria

The cohesive elements three damage initiation criteria, s_n^o, s_s^o and s_t^o, must be defined to ensure that the fracture process is initiated. The nominal tensile damage initiation criterion (s_n^o) is set as an arbitrary and considerably high value ($10 \cdot 10^6$ MPa). This is to make sure that the fracture will propagate as a pure mode II fracture and not as mode I or a combination.

The nominal shear damage initiation criterion for mode II fracture (s_s^o) is set to 1 MPa. As long as the value is less than the element's yield stress, it does not affect the fracture load. The initiation criterion for mode III fracture (s_t^o) is not relevant for the given load situation, and is also set to 1 MPa.

Critical energy release rate

The cohesive model is now able to simulate correct stresses in the bondline and the damage criteria are defined, this means that we can now try to simulate fracture in the elements. The critical energy release rate is, however, still unknown. To define the right energy release rate the joint with the 3 mm CFRP overlap was assumed to have a failure load of 71.2 kN, this load is based on the measured failure loads from the MARSTRUCT project. A critical energy release rate for mode II fracture (Γ_{cs}) was then determined so the FE model of the joint would fracture at the measured failure load. The critical energy release rate was determined to be $5040\,\frac{J}{m^2}$.

This value is assumed to be a material property of the adhesive and is used in all simulations discussed in the present thesis.

Table 4.4 presents a summary of the material properties chosen for the cohesive elements.

Table 4.4: Material properties for the cohesive elements

	Araldite 2015
Element stiffness for mode 1 failure, K_{nn} [GPa]	2600
Element stiffness for mode 2 failure, K_{ss} [GPa]	1600
Element stiffness for mode 3 failure, K_{tt} [GPa]	1600
Shear yield stress, τ_y [MPa]	20
Damage initiation for mode 1 failure, s_n^o [MPa]	$10 \cdot 10^6$
Damage initiation for mode 2 failure, s_s^o [MPa]	1
Damage initiation for mode 3 failure, s_s^o [MPa]	1
Critical energy release rate (mode independent), Γ_c [J/m^2]	5040

The material properties presented in this section are used in all FE models in the present thesis unless other is specified.

The model is now capable of simulating the behaviour of the adhesive in a satisfying manner, both general material behaviour and, at high loads, degradation and fracture. The importance of an accurate representation of the adhesive cannot be overemphasized, and is essential for simulating patch repair.

The DBS joint is now suitable to be modified to a single-edge notched tension steel plate reinforced with CFRP patches.

4.2 Single-edge notched steel plate

This section covers the modelling and analysis of a single-edge notched steel plate with double-side CFRP reinforcement (double-sided patch repair) in Abaqus. The model is based on the DBS joint presented in Section 4.1. It shares its element selection, constraints, material properties, and to some extent its geometry.

The main objective is to successfully analyse the stress intensity at the crack tip of the tension loaded steel plate, with and without CFRP patches. And to perform a parametric study investigating the effects of

- different crack lengths
- different overlap widths
- different overlap thicknesses
- patch placement

4.2.1 Model Geometry

The model's geometry is presented in Figure 4.6. It consists of five parts: a cracked steel plate, two adhesive layers and two CFRP patches.

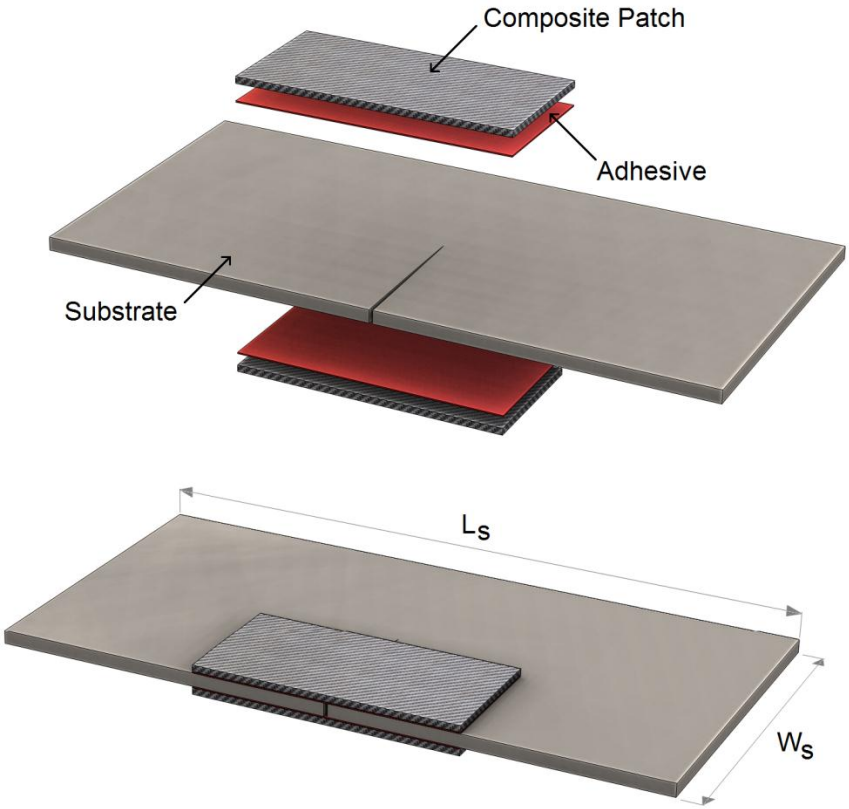

Figure 4.6: Single-edge notched steel plate – Model geometry.

The stress intensity factor *K* is calculated directly in Abaqus, and if the crack is defined on a symmetry plane, as it is in our situation, only half the structure needs to be modelled. Hence, the full size model from Figure 4.6 can therefore be cut in half to minimize computational costs. The reduced model is illustrated below in Figure 4.7.

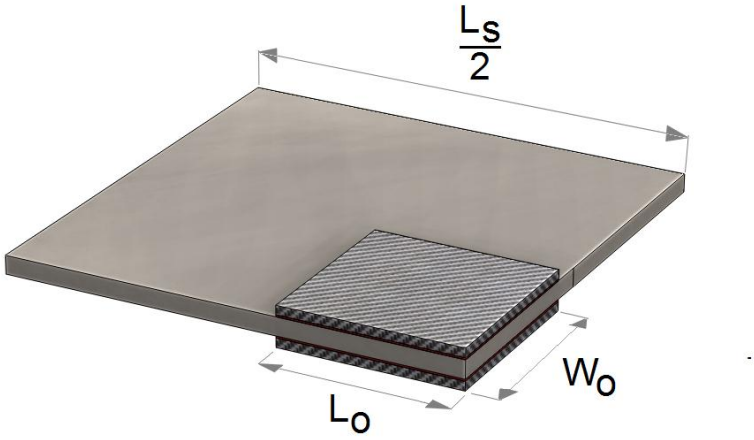

Figure 4.7: Single-edge notched steel plate – Reduced model.

The CFRP patches have an overlap length, L_o = 300 mm, and variable width, W_o, and thickness, t_o. The adhesive layer has a fixed thickness, t_a = 0.5 mm.

The steel plate has the following dimensions

- thickness, t_S = 21 mm
- length, L_S = 5200 mm
- width, W_S = 1500 mm
- and a variable crack length, a.

The thickness of the steel plate, t_S, is to equal the thickness of the ship deck that will be discussed in Chapter 5. The length of the plate, L_S, is chosen in order to be sufficiently long so it does not influence the stress intensity at the crack tip. An arbitrarily width, W_S, is chosen for the plate.

4.2.2 Modelling and meshing of the crack tip

The onset of cracking in Abaqus can be studied for quasi-static problems by the evaluations of contour integrals.

In a FE model each evaluation can be thought of as the virtual motion of a block of material surrounding the crack tip. Each block is defined by contours, where each contour is a ring of elements completely surrounding the crack tip or, in a three dimensional model, the nodes along the crack line from one crack face to the opposite crack face. These rings of elements are defined recursively to surround all previous contours (Dassault systèmes, 2012). Figure 4.8 illustrates a crack tip with a focused mesh and two surrounding contours.

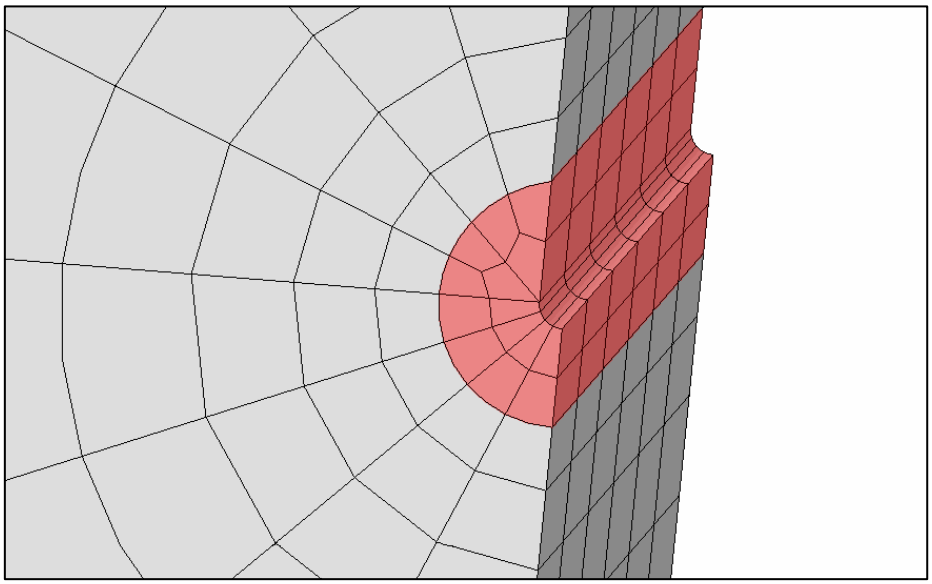

Figure 4.8: Two contours surrounding a crack tip in a focused mesh.

The method requires that the user adapts the mesh to the cracked geometry, to explicitly define the crack front, crack line and to specify the virtual crack extension direction. The crack front is the forward part of the crack. Abaqus uses the crack front to compute the first contour integral using all of the elements inside the crack front and one layer of elements outside the crack front.

A detailed focused mesh is generally required and for typical problems, the most efficient mesh design for the crack tip region has proven to be the “spider web” configuration (Anderson, 2005), which consists of concentric rings of elements that are focused toward the crack tip. The spider web design enables a smooth transition from a fine mesh at the tip to a coarser mesh at a more remote distance. The rings surrounding the crack tip are perfect for integration contours.

Figure 4.9 displays the crack tip meshing used in the model, as one can imagine the meshing is rather time consuming.

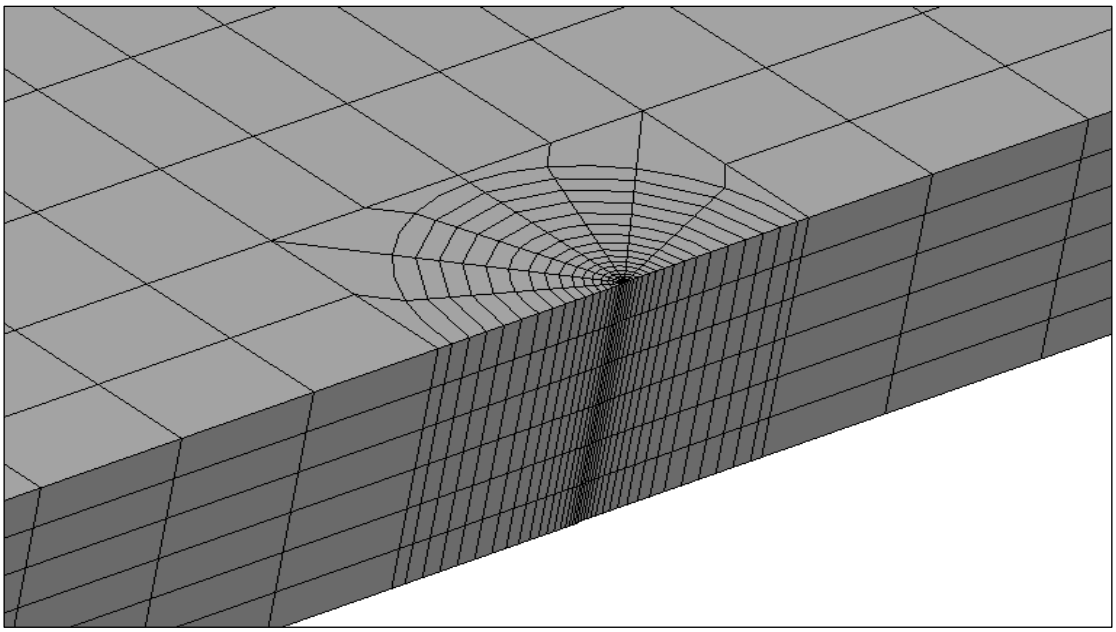

Figure 4.9: Spider web pattern mesh.

At first, a mesh with square contours were modeled (illustrated in Figure 4.10), but the accuracy of the results acquired from the contour integrals were so poor that the mesh were remodeled in to the spider web design.

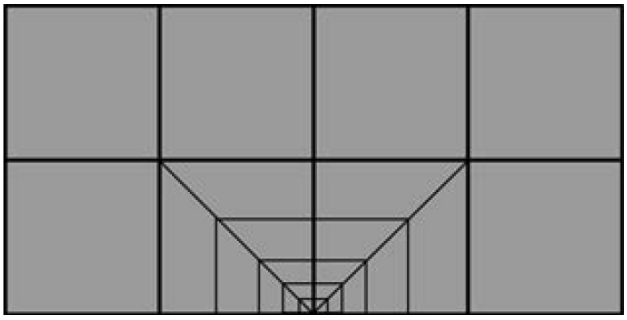

Figure 4.10: Mesh with square contours (Anderson, 2005).

When a suitable mesh is established, Abaqus automatically finds the elements that form each ring surrounding the defined crack front. Each contour provides an evaluation of the contour integral. The possible number of evaluations is the number of such rings of elements.

There are several types of contour integrals. The integral chosen for this model is the *J*-integral, which can be defined to calculate the stress intensity factor, *K*.

The *J*-integral

The *J*-integral is usually used in quasi-static fracture analysis to characterize the energy release associated with crack growth, but it can be related to the stress intensity factor if the material response is linear.

The *J*-integral is defined in terms of the energy release rate associated with crack advance. For a virtual crack advance $\lambda(s)$ in the plane of a three-dimensional fracture, the energy release rate is given by

$$\bar{J} = \int_A \lambda(s)\mathbf{n} \cdot \mathbf{H} \cdot \mathbf{q} dA \tag{4.1}$$

where dA is a surface element along a vanishing small tubular surface enclosing the crack tip or crack line, $\mathbf{n}$ is the outward normal to dA, and $\mathbf{q}$ is the local direction of virtual crack extension. $\mathbf{H}$ is given by

$$\mathbf{H} = \left(W\mathbf{I} - \boldsymbol{\sigma} \cdot \frac{\partial \boldsymbol{u}}{\partial \boldsymbol{x}}\right) \tag{4.2}$$

For elastic material behaviour *W* is the elastic strain energy; for elastic-plastic or elasto-viscoplastic material behaviour *W* is defined as the elastic strain energy density plus the plastic dissipation, thus representing the strain energy in an "equivalent elastic material" (Dassault systèmes, 2012).

For linear elastic materials, $\bar{J} = \Gamma$, hence

$$\bar{J} = \frac{K^2}{E'} \tag{4.3}$$

4.2.3 Loading and boundary conditions

The steel plate is loaded with a uniform negative pressure, $S = 117{,}5\ \mathrm{MPa}$.

The symmetry plane of the steel plate and patches (collared red in Figure 4.11) are assigned symmetry boundary conditions about the x-plane. This restrains the surface from movement in the x-direction and from rotating around the y- and z-axes.

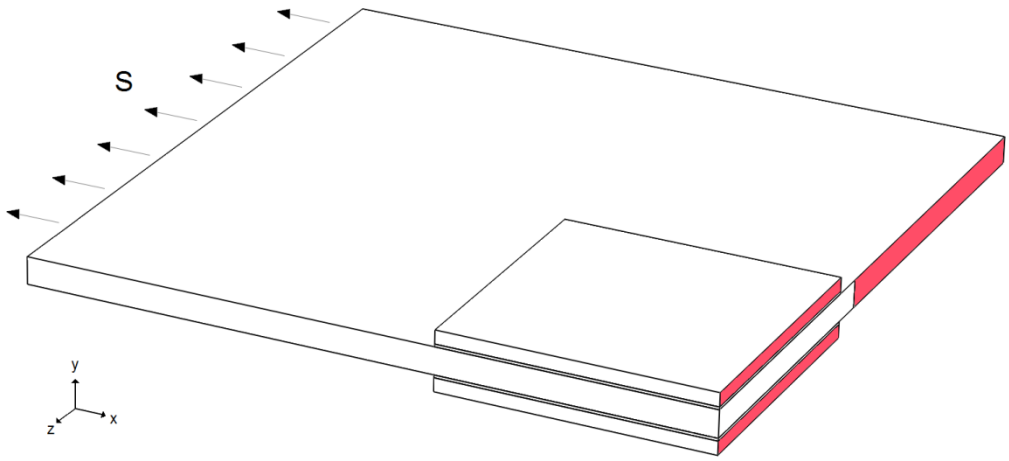

Figure 4.11: Loading and boundary conditions

Performance of the SENT model and results are presented and discussed in Chapter 6.

Chapter 5

Fatigue life estimation for a crack emanating from a ship manhole

Vessels used by the offshore oil and gas industry, such as shuttle tankers and floating production, storage and offloading units (FPSOs), are often operating in harsh conditions and can be subjected to severe wave loadings, which result in high cyclic stresses. This constant fatigue loading and the amount of fatigue critical details throughout the ships make these types of structures very disposed to fatigue cracking.

Ships can normally limit the amount of large fatigue loading by scheduling a passage to avoid the most severe storms. By avoiding the most extreme fatigue loading, the life of a ship can be increased significantly. For some vessels, however, such as FPSO's and FSO's (floating storage and offloading units) that are moored to the seabed, severe storms cannot be avoided and the extent of fatigue cracking increases.

Since the mentioned vessels are either transporting, processing and/or storing hydrocarbons, repairs that include hot work (and the risk of fire) must be avoided when the ship is in service. A shutdown of production to perform unscheduled maintenance has large economic consequences. A cold repair option, such as composite patch repair, is therefore highly relevant for these types of ships, at least as a temporary solution. A repair is much more affordable if it can be delayed and scheduled in with other planned work.

A feature on ships that commonly experiences growth of cracks is manholes. Manholes are prone to fatigue crack growth since the tensile stress near a hole (in an infinite wide plate) is three times higher than the plate's nominal stress. For finite plates the stress concentrations are even higher. In the present chapter, a case study on how CFRP patches can reduce the growth of a crack emanating from a manhole on the upper deck on a shuttle tanker will be perform. The manhole will be modelled with two different patch repair alternatives. First, a double sided patch on the main deck, then a patch on the inside of the rim of the manhole. The main objective is to estimate the amount of cycles (under constant amplitude loading) required for the crack to grow from its initial size a_i to a final size $a_{f_{„}}$ with and without CFRP patches, and to compare the two patch repair alternatives.

5.1 Double sided patch repair

5.1.1 Model Geometry

The shuttle tanker in question has a crack growing from a manhole at the upper deck, as shown below in Figure 5.1. The crack is estimated to have an initial size a_i of 105 mm. To ease the modelling process and make the study more general, the surrounding geometry of the manhole is reduced to a simple wide plate, excluding stiffeners, bulkheads and so on. This simplification of the model will also make it possible to compare the results from Abaqus (without patches) to existing empirical solutions. In this way the accuracy of the model can be verified.

Figure 5.1: Crack growing from a manhole at upper deck.

The FE model is based on the single-edge notched tension steel plate modelled in Chapter 4, it shares its main mesh, constraints, material properties and element selection. The crack tip and its spider web mesh are identical.

The model geometry is illustrated in Figure 5.2 and Figure 5.3. The crack is defined on a symmetry plane so only half the structure needs to be modelled.

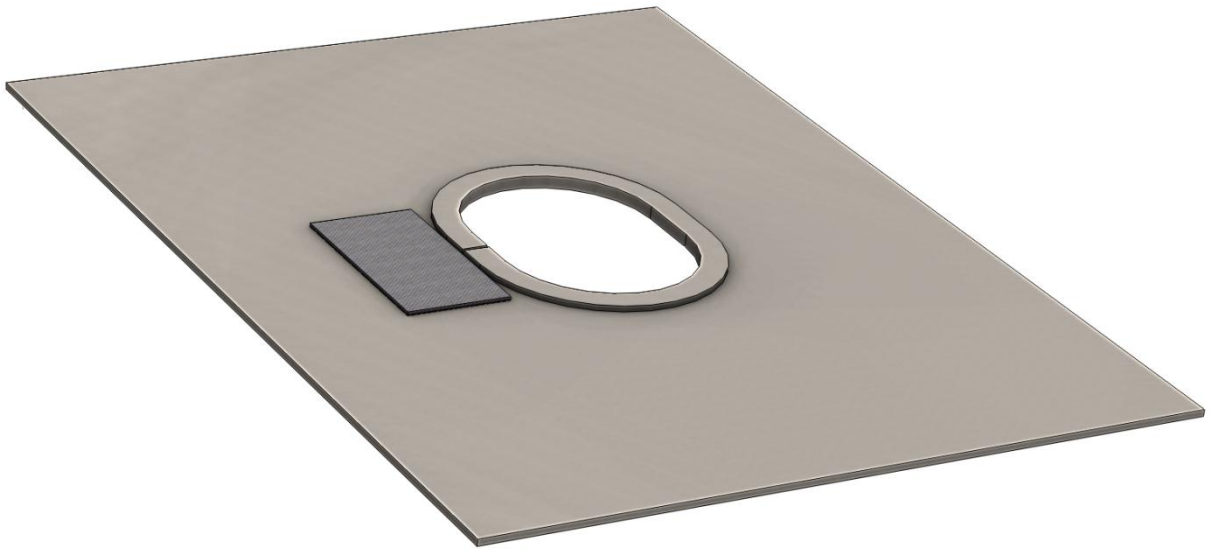

Figure 5.2: Double sided patch repair – Full size model

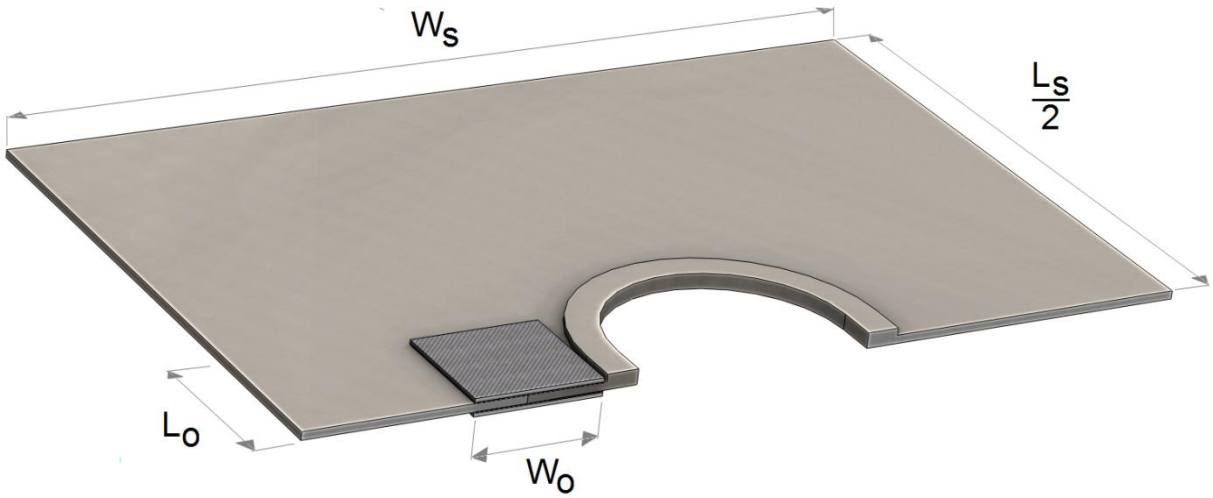

Figure 5.3: Double sided patch repair – Reduced model

The model has the following dimensions:

CFRP patches:

- thickness, t_o = 6 mm
- overlap length, L_o = 300 mm
- width, W_o = 325 mm

Steel plate:

- thickness, t_S = 21 mm
- length, L_S = 7800 mm
- width, W_S = 3980 mm
- and a variable crack length, a.

(The motivation for choosing these specific dimensions for the steel plate will be discussed in Section 5.1.3.)

Adhesive layer:

- thickness, t_a = 0.5 mm

Manhole:

- Manhole, 800x600 mm
- Liner thickness, 18 mm
- Liner width, 80 mm

At first, the liner on top of the manhole was included in the model, but the asymmetry of the cross section made the deck bend under loading, as shown in Figure 5.4. This bending of the deck was believed to lead to peel stresses in the adhesive that could reduce the capacity of the joint and eventually cause delamination. Since the cohesive elements are not defined to simulate Mode I fracture, it was considered to exclude the liner from the model in order to prevent the deck from bending. Stress analysis of the adhesive layers showed, however, that the adhesive were little affected by the liner and that it did not cause excessive peel stresses.

Although the liner did not affect the stress situation in the adhesive layers, as first thought, it did to a large extent effect the running time of the model and was, in order to save computational costs, removed from the model.

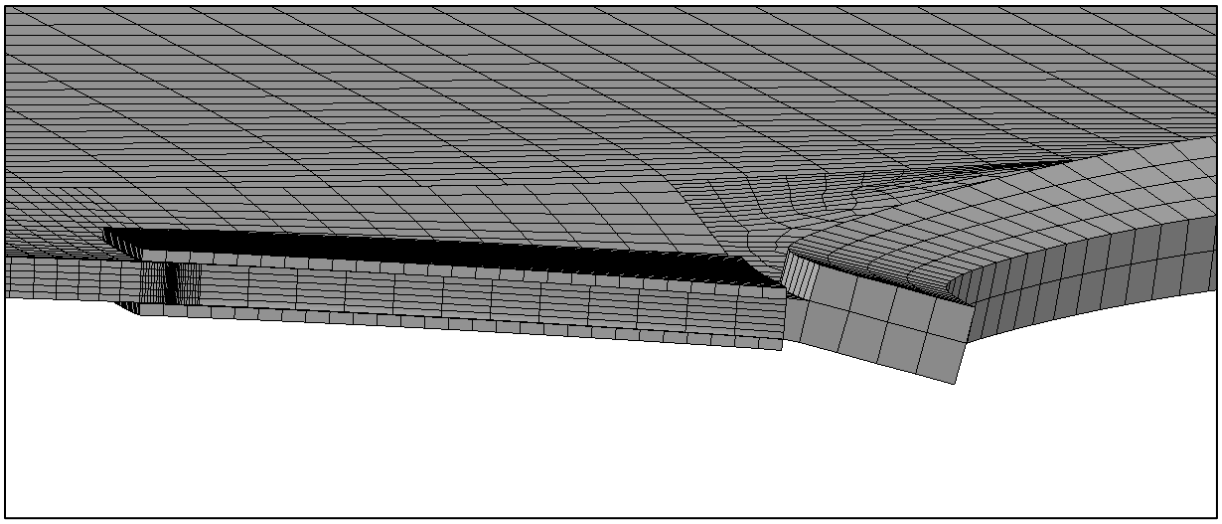

Figure 5.4: Bending of manhole with liner at the applied load of 50 MPa. Deformation scale factor = 100.

5.1.2 Loading and boundary conditions

The deck is loaded with a uniform negative pressure. It's assumed that the upper deck of the shuttle tanker experiences an average fatigue stress range Δ*S* of 50 MPa. The loading is regarded as zero-to-tension ($R = 0$) with constant amplitude.

The symmetry plane of the deck and patches (colored red in Figure 5.5) are assigned symmetry boundary conditions about the x-plane. This restrains the surface from movement in the x-direction and from rotating around the y- and z-axes.

The faces colored green in Figure 5.5 are assigned symmetry boundary conditions about the z-plane. This restrains the surface from movement in the z-direction and from rotating around the x- and y-axes.

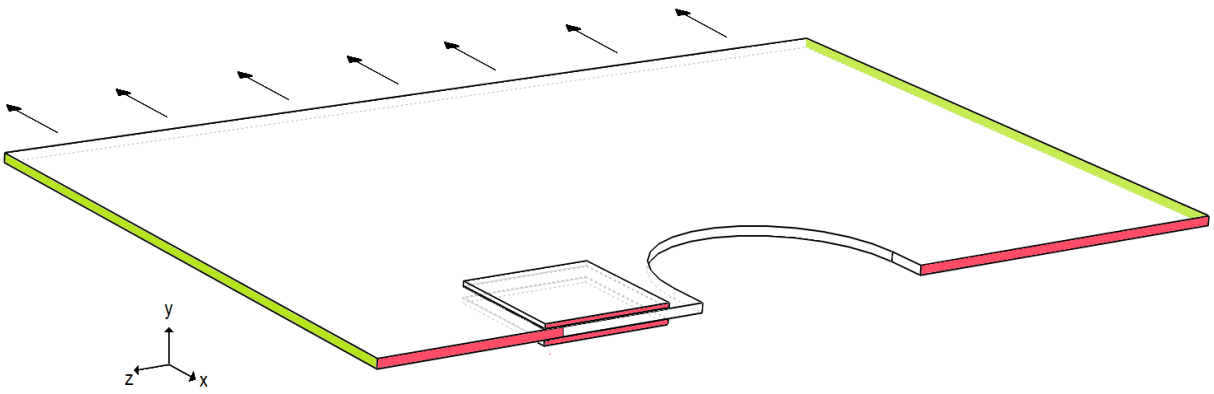

Figure 5.5: Loading and boundary conditions.

5.1.3 Effect of limited model size

The stress intensity factor of the crack tip depends, as discussed in Section 2.1.1, on the width and length of the plate. Less width and length leads to a higher stress concentration at the tip of a crack. W_S and L_S are therefore chosen to be sufficiently large so the plate's outer limits have minimum effect on the stress intensity factor without largely increasing the computational costs. To decide on the extent of the plate and to verify the correctness of the stress intensity calculated by Abaqus, the results were compared to *F* factors defined by Paris and Sih for an infinite plate with a circular hole. The model is, however, not directly comparable to the *F* factors established by Paris and Sih since the manhole has the shape of an elongated circle. This shape should, at least for short crack lengths, reduce the stress intensity to some extent.

Figure 5.6 displays the *F* factors established by Paris and Sih.

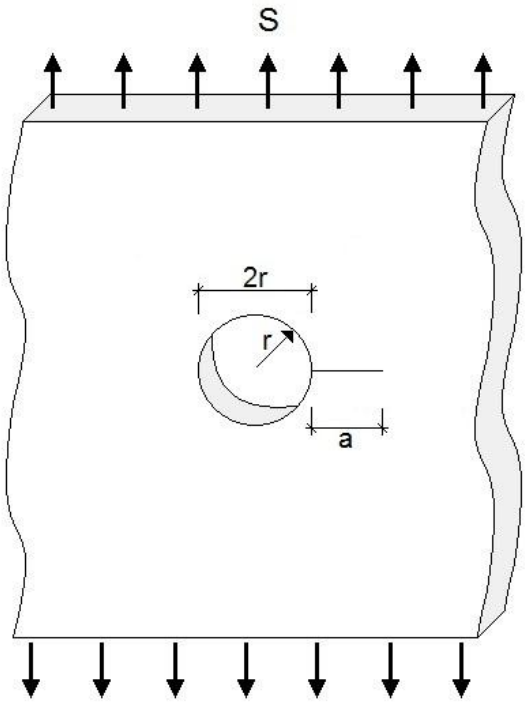

$$K = F(a/r)S\sqrt{\pi a}$$

(a/r)	$F(a/r)$
0	3,39
0,1	2,73
0,2	2,3
0,3	2,04
0,4	1,86
0,5	1,73
0,6	1,64
0,8	1,47
1	1,37
1,5	1,18
2	1,06
3	0,94
5	0,81
10	0,75
∞	0.707

Figure 5.6: *F* factor for cracks emanating from a circular hole in an infinite plate (Paris & Sih, 1964).

Figure 5.7 displays a chart comparing the empirical solution with results from the FE analyses. In order to include the effect of a state of plain strain near the tip of the crack, *F* factors obtained by the empirical solution are multiplied by a factor $(1-\nu^2)^{-0.5}$ (see Section 6.1.1).

The plot shows relatively good agreement between the two approaches. *F* factors obtained by Abaqus are, as expected, slightly smaller since an elongated hole results in less intense stress concentrations than a circular hole. The deviation declines from 4.2 % to 0.2 % as the crack length increases. The difference decreases as the crack itself becomes a more dominant stress raiser and the effect of the hole decreases. The decreasing difference is, possibly, also due to the limited extent

of the Abaqus model, which becomes more significant as the distance from the crack tip to the edge of the plate decreases as the crack grows.

The stress raising effect of the plate's edge can be reduced by extending the limits of the model. Extending the model will, however, lead to increased computational costs, which is unwanted as the analyses already are rather time consuming.

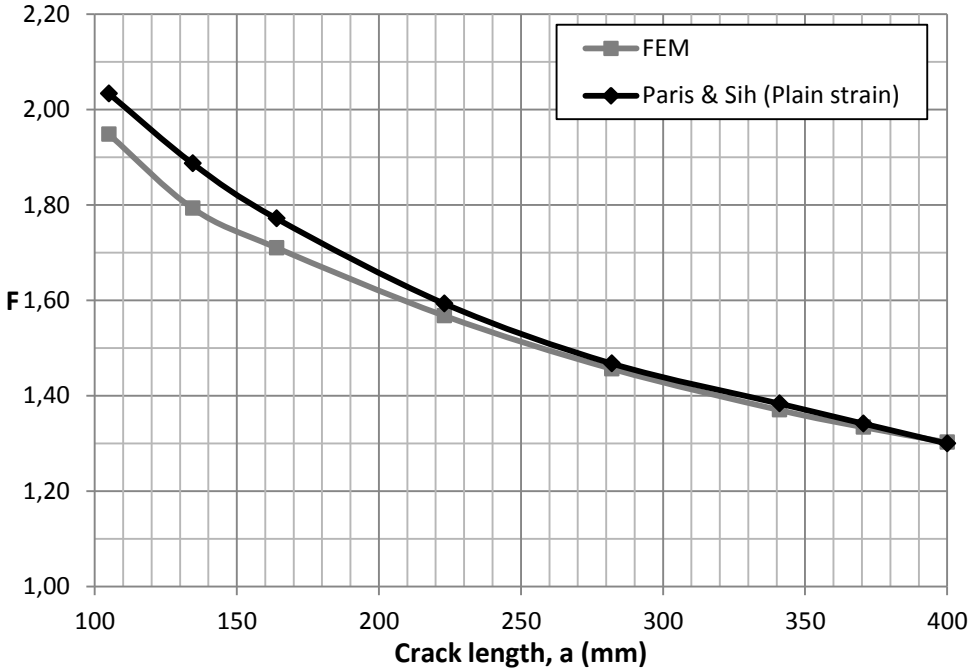

Figure 5.7: Comparison of F factors established by Paris & Sih and F factors calculated by FE analyses.

5.1.4 Life estimation

The main objective of the analyses is to estimate the amount of cycles required for the crack to grow from its initial size a_i to a final size a_f, with and without CFRP patches.

For life estimates, the final crack size a_f is usually chosen as the critical crack length a_c, where the value of K_{max} has reached the critical stress intensity factor, K_C (as described in Section 2.5.3). At this point the stress intensity at the crack tip is so severe that a full failure is expected. The critical crack length can be expressed by the following equation

$$a_c = \frac{1}{\pi}\left(\frac{K_{IC}}{FS_{max}}\right)^2 \tag{5.1}$$

For the given situation the material fracture toughness is unknown and the calculated *F* factors are likely to be fairly exaggerated due to the simplification of the model. The conservativeness of the

model would therefore have led to an unlikely short estimated critical crack length. The final crack length is, for those reasons, a selected value of 400 mm.

The crack's initial size a_i is estimated to be 105 mm.

We know from Section 2.5.2 that the amount of cycles needed for a crack to grow from its initial length a_i, to its final length a_f, can be estimated by the following integral

$$N_{if} = \int_{N_i}^{N_f} dN = \int_{a_i}^{a_f} \frac{1}{C(\Delta K)^m} da \qquad (5.2)$$

where ΔK can be expressed as follows

$$\Delta K = F \Delta S \sqrt{\pi a}$$

I our case, F_i and F_f (corresponding to a_i and a_f) differ to such an extent, both for the situation with and without patches, that F must be treated as a variable, hence numerical integration is needed.

A simple method of numerical integration is Simpson's rule. Simpson's rule is based on the assumption that a parabola passes through three neighbouring points, as illustrated in Figure 5.8.

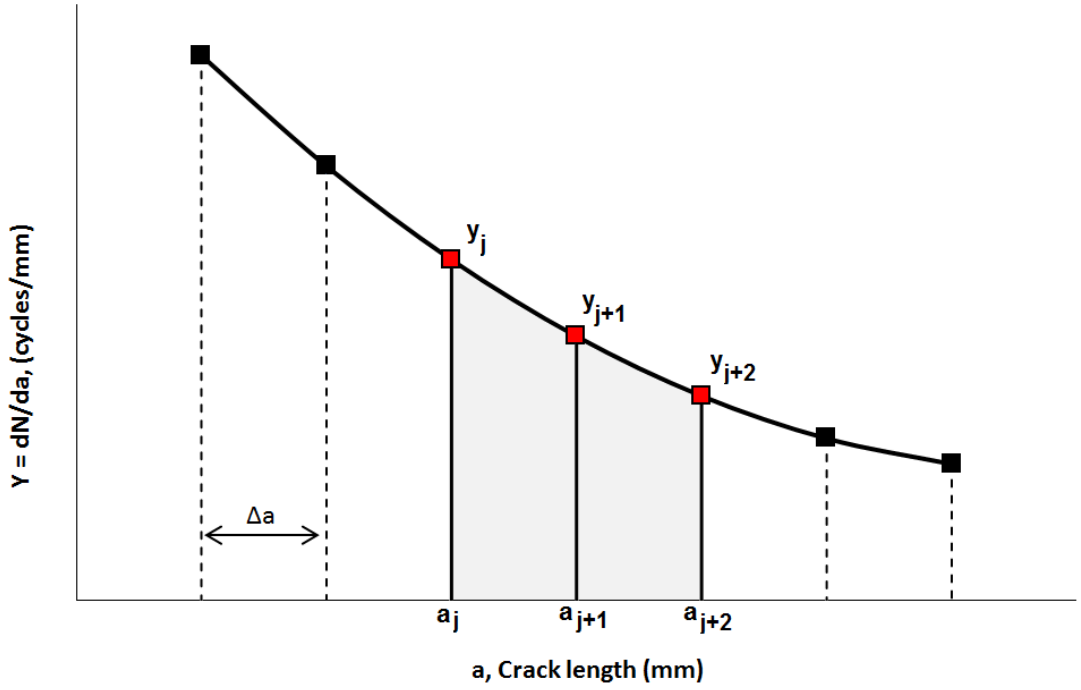

Figure 5.8: Area under the dN/da versus a curve over two intervals of Δa as estimated by Simpson's rule (Dowling, 2012).

To increase the accuracy of the method, the integral can be broken up into a number of small intervals. Summing up the contributions from each calculation gives an approximate value of the total area, and in our case, the number of cycles N_{if}. If the points are equally spaced Δa apart, the area estimate is

$$\int_{a_j}^{a_{j+3}} y\, da = \frac{\Delta a}{3}(y_j + 4y_{j+1} + y_{j+2}) \qquad (5.3)$$

To apply the Simpson's rule, the stress intensity range ΔK in the two models, with and without CFRP patches, must be calculated for different crack lengths ranging from a_i to a_f. Seven different crack lengths for the two models were chosen. In the region where most of the area, and thus most of the cycles are accumulated, the interval between the lengths was halved in order to increase accuracy. This region is near a_i for the model with no patches and near the finial length a_f for the model with patches.

Table 5.1 displays the chosen crack lengths, a, and the corresponding crack length intervals, Δa.

Table 5.1: Simulation plan with crack lengths and corresponding Δa.

No patch		**6 mm double patch**	
a (mm)	**Δ*a*** (mm)	***a*** (mm)	**Δ*a*** (mm)
105		105	
	29,5		59
134,5		164	
	29,5		59
164		223	
	59		59
223		282	
	59		59
282		341	
	59		29,5
341		370,5	
	59		29,5
400		400	

5.1.5 Material properties

The deck of the ship is constructed with higher-strength ABS shipbuilding steel, type AH36. The steel's material properties are presented in Table 5.2.

Table 5.2: AH36 steel material properties (ASTM Int., 2008).

	AH36 steel
Young's modulus [GPa]	206
Poisson's ratio	0.3
Yield strength [MPa]	355
Ultimate tensile strength [MPa]	490-620

The Paris law material constants, C and m, are chosen for Ferritic-pearlitic type of steel from Table 2.1, $C = 6.89 \cdot 10^{-9}$ and $m = 3.0$. These apply under zero-to-tension loading when $R = 0$.

Results from analyses of the model are presented and discussed in Chapter 6.

5.2 Single patch repair inside rim

Applying patches on each side of the deck may not be possible; an alternative option is to place a patch inside the rim of the manhole. This alternative will be presented in the present section.

5.2.1 Model Geometry

The model's main geometry is as presented in Section 5.1.1, except now a CFRP patch is placed on the inside of the rim of the manhole instead of the two patches on each side of the deck. The placement of the patch is illustrated in Figure 5.9.

Figure 5.9: Illustration of manhole with patch inside liner

The liner on top of the manhole was not included in the model with the double sided patch repair. For this configuration the liner must be included to create a larger bonding area for the patch. The width of the bondline is 39 mm with the liner included. The patch thickness is still 6 mm.

The overlap length is 336 mm and is sufficient to be characterized as a long overlap. This particular length is chosen because it is, for the given configuration, advantageous in terms of modelling.

5.2.2 Loading and boundary conditions

The deck is experiencing the same loading and boundary conditions as presented in Section 5.1.2. Additionally, the whole surface underneath the deck is restrained from movement in the vertical direction parallel to the y-axes. The additional boundary condition is assigned the model in order to

prevent the deck from bending. Attempts were made to run the model without this extra restraint, but they were unsuccessful.

It was tried to limit the patch to the area of the rim that is not curving, hence overlapping the crack with 100 mm on each side. The attempt was successful in terms of the being able to run the analysis, but the overlap length of 100 mm proved to be insufficient. The configuration can be defined as a joint with short overlap length; hence the patch capacity is proportional to the length of the overlap.

The shear stress distribution along the bondline at different applied load levels is presented in Figure 5.10. The analysis has been performed on the initial crack length, a = 105 mm.

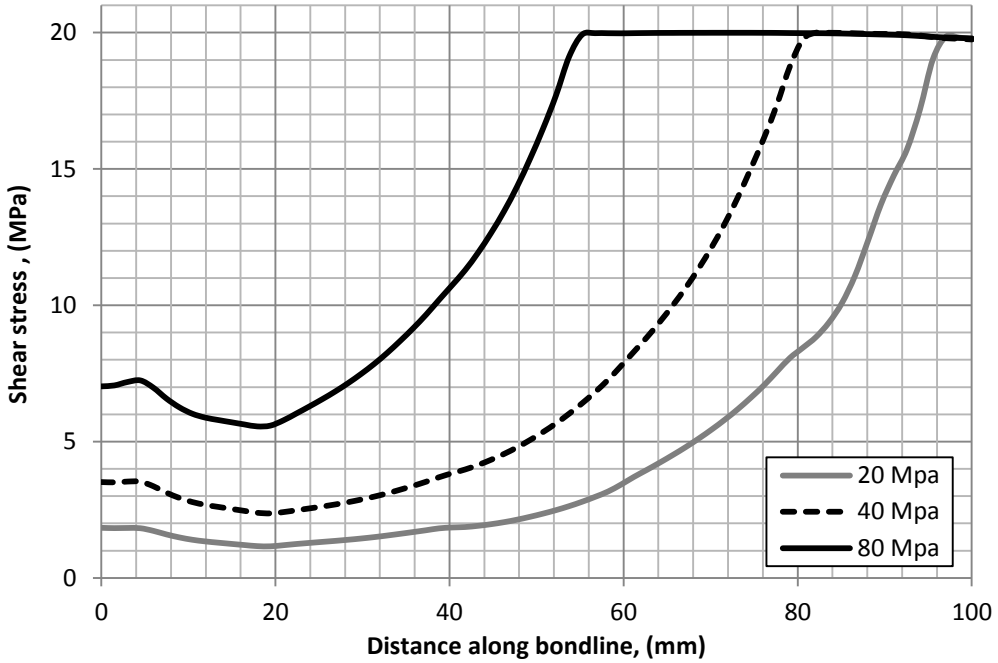

Figure 5.10: Shear stress along the bondline at various loads, a = 105 mm.

The mechanical response is linear elastic at low load levels. As the load increases, the right side of the bondline becomes plastic. The plastic area continues to grow as the load increases until the whole bondline is fully plastic. This is consistent with the theory for short overlaps presented in Section 3.2. Reducing the length of the overlap was therefore not an option.

Chapter 6

Results and discussion

The main objective of the present thesis is to study how CFRP patches can reduce the stress intensity at the crack tip in cracked steel plates, and how these patches, by reducing the stress intensity, can limit the extent of fatigue crack growth.

In order to do the above, a single-edge notched tension (SENT) steel plate and a cracked ship manhole have been modelled and analysed, with and without CFRP patches. The present chapter contains a presentation of the results obtained from the FE analyses.

First, results from the FE model of the SENT steel plate will be presented, and then results from the model of the manhole. All the presented results will be discussed along the way.

6.1 SENT steel plate with CFRP reinforcement

A single-edge notched steel plate has been modelled in the finite element software Abaqus, with and without double-sided CFRP reinforcement.

The main objective of the modelling was to successfully analyse the stress intensity at the crack tip, and study how CFRP patches could reduce the stress intensity and consequently prevent the crack from growing.

A parametric study has been undertaken in order to investigate the influence of

- different crack lengths
- different overlap widths
- different overlap thicknesses
- patch placement

First in this section, the performance of the finite element model will be compared to empirical formulas to make sure that the results are reliable. Then the results from the parametric study will be presented and discussed.

At the end of the section, a short summary will be presented.

6.1.1 Comparison between the FE model and empirical solutions

A comparison between the FE model and an empirical formula is undertaken in order to make sure that the model is accurate.

Figure 6.1 displays the *F* factors for the cracked steel plate without CFRP patches calculated respectively with the finite element method and an empirical formula from "*The stress analysis of cracks handbook*" (Equation (2.6)).

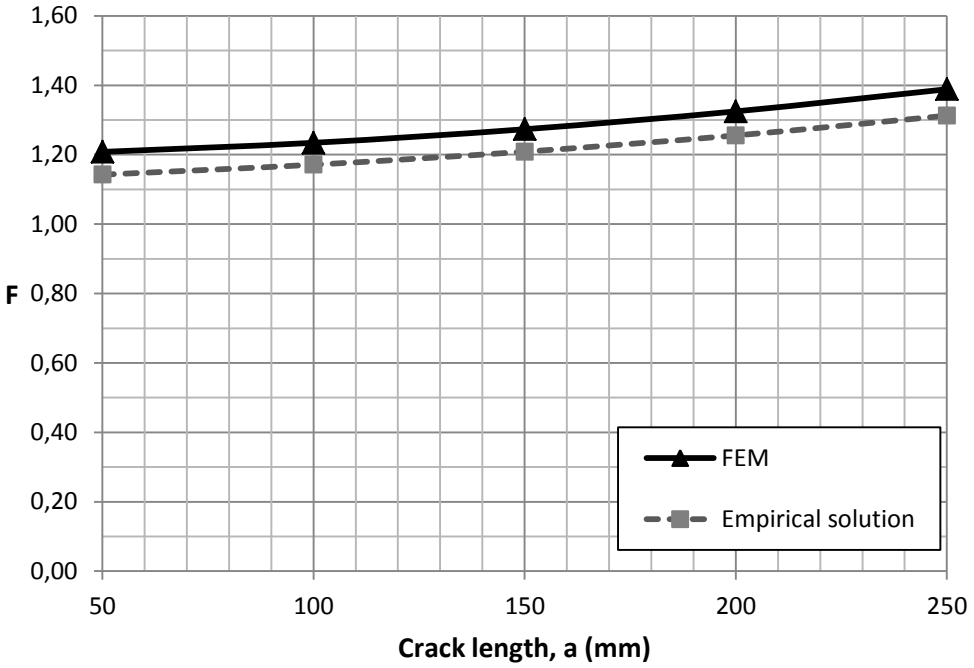

Figure 6.1: A comparison of the *F* factors calculated by FEM and an empirical solution.

The results are plotted for crack lengths varying from 50 mm to 250 mm. The two methods are displaying a parallel development as the crack grows. The *F* factors obtain by Abaqus are, however, about 5 % to 6 % larger than the ones calculated with the empirical formula.

The reason for this was at first uncertain and a number of analyses were performed to find the cause of it. The high *F* factors were thought to be the result of insufficient plate length, incorrect boundary conditions or in some way caused by inadequate meshing.

The reason for the difference between the two methods is not related to any of the above, but can be explained looking at the plate's state of stress.

Solutions reported in stress intensity handbooks are generally based on the assumption of a thru thickness state of plain stress. Many of these solutions are obtain by finite element analyses, but these have mostly been limited to two-dimensional problems. Stresses are, however, not uniform through the thickness, and can only be accurately analysed using three dimensional analyses (Y. Yamamoto, 1978).

Bakker showed by performing three-dimensional FE analyses that a cracked plate under plane stress undergoes a change to plane strain behaviour near the crack tip (Bakker, 1992). This behaviour occurs since the crack tip is loaded to higher stresses than the surrounding material. Because of large stresses normal to the crack plane, the crack-tip material tries to contract, but is prevented from doing so by the surrounding material. This local constraint causes plane strain behaviour near the crack tip (Anderson, 2005), and an increase in stress intensity which is neglected in analyses that assumes a constant state of plain stress.

The contour integral in Abaqus reports $\bar{J}$ and additionally calculates the stress intensity factor directly. Figure 6.2 compares the stress intensity factor calculated by Abaqus, and *K* calculated from the value of $\bar{J}$ with the assumption of plain strain and plain stress. The stress intensity factor calculated by the empirical formula is also presented.

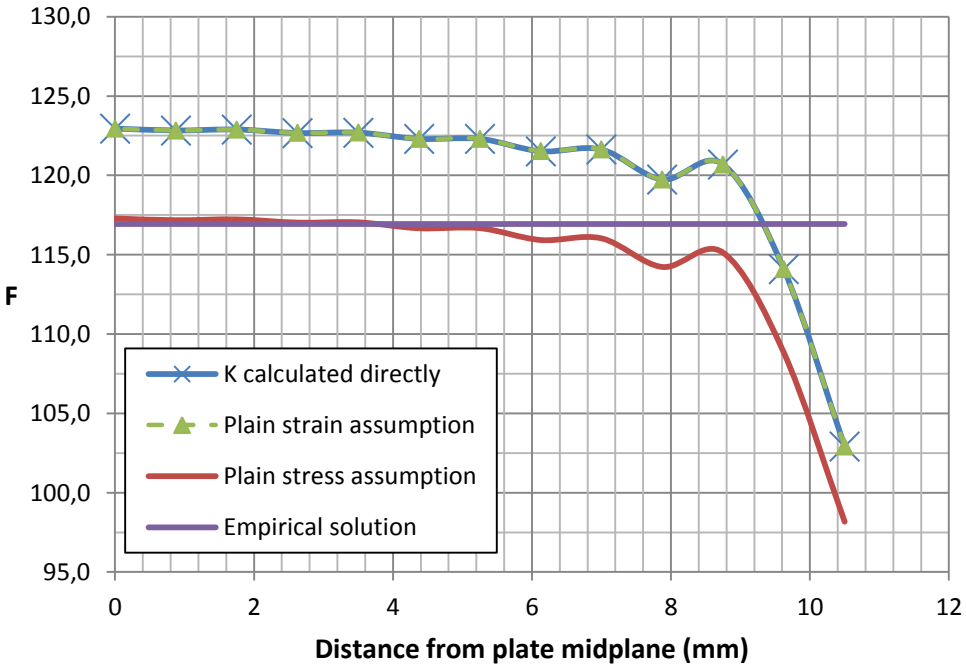

Figure 6.2: Comparison of *K* calculation methods for plane strain and plane stress assumptions for a 200 mm crack.

It can be seen from the plot, that *K* values calculated directly by Abaqus match closely to the values calculated from $\bar{J}$ when assuming plane strain. This is consistent with the findings of Bakker that demonstrated a state of plane strain near the crack front (Bakker, 1992).

It can also be seen that the empirical solution matches the stress intensity calculated with the assumption of plain stress. In other words, the empirical formula is underestimating the stress intensity by a factor $(1-\nu^2)^{-0.5}$ (see Equation (2.7)).

Figure 6.3 displays a comparison of the *F* factors for the cracked steel plate without CFRP patches calculated with the finite element method, and the empirical formula where *F* is multiplied by the factor presented above.

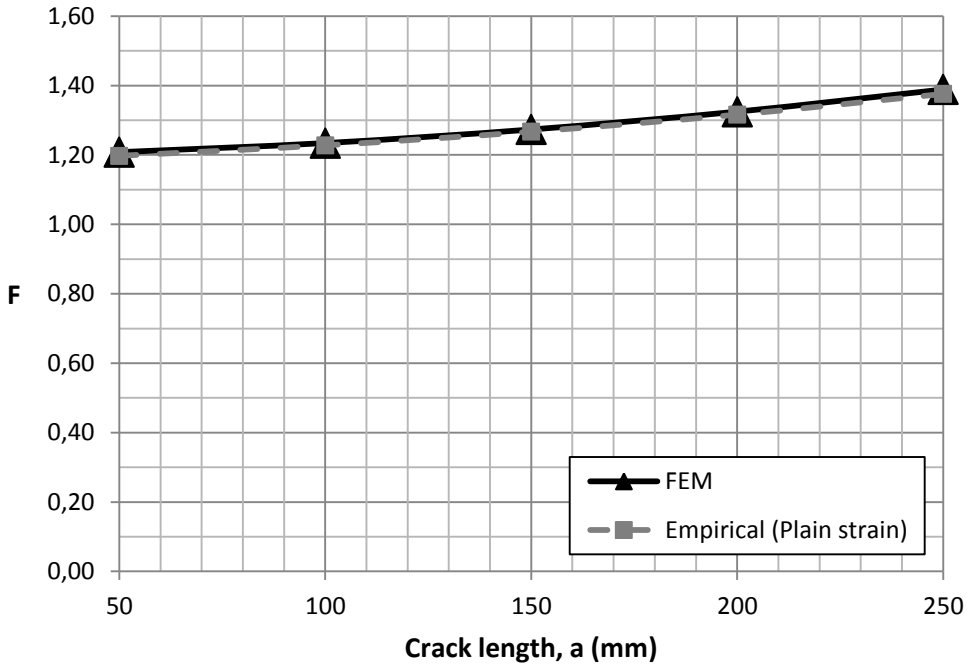

Figure 6.3: A comparison of the *F* factors calculated by FEM and an empirical solution where a state of plain strain taken into account.

As we can see, are the two methods now showing good agreement, and the finite element model appears to be performing in a satisfying manner.

6.1.2 Reduction of stress intensity factors

In order to investigate to what extent composite patches are able to reduce the stress intensity at the crack tip, the cracked plate has been analysed with 3 mm and 6 mm CFRP patches for various crack lengths.

The stress intensity factors obtained from the analyses are, in Figure 6.4, compared to stress intensity factors from a model without patches.

The patches are for all crack lengths modelled with a 300 mm long and 265 mm wide overlap. The composite patches overlap the crack tip by 15 mm for the longest crack length (250 mm).

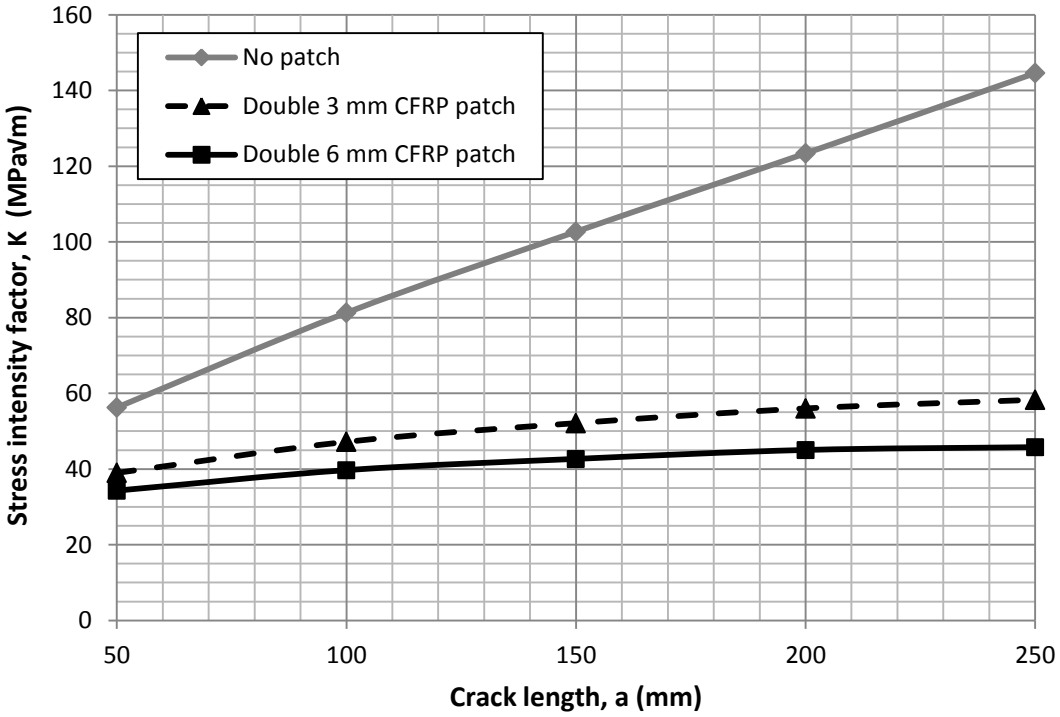

Figure 6.4: Comparison of stress intensity factors.

Figure 6.4 shows that by decreasing the stress field at the crack tip, the stress intensity factors can be effectively reduced by CFRP reinforcement. *K* for the patched configurations appears to even out at a low value. While the stress intensity for the unpatched configuration, on the other hand, keeps escalating as the crack propagates.

With a 3 mm CFRP doubled sided patch, the stress intensity factors are reduced by 32 % to 60 % for crack lengths between 50 and 250 mm. By increasing the thickness of the patch from 3 mm to 6 mm one obtains a further reduction of about 9 %.

Table 6.1 presents the results plotted in Figure 6.4 in a tabular form.

Table 6.1: Reduced stress intensity factors for the cracked plate with 3 mm and 6 mm CFRP patches

Crack length	**No patch**	**3 mm CFRP**		**6 mm CFRP**	
a (mm)	K $(\mathrm{MPa}\sqrt{m})$	K $(\mathrm{MPa}\sqrt{m})$	Reduction	K $(\mathrm{MPa}\sqrt{m})$	Reduction
50	56,3	39,0	31,7 %	34,3	39,0 %
100	81,3	47,2	42,0 %	39,7	51,1 %
150	102,7	52,1	49,2 %	42,7	58,4 %
200	123,4	56,0	54,6 %	45,0	63,5 %
250	144,6	58,3	59,7 %	45,8	68,3 %

6.1.3 Overlap width and placement

A study has been undertaken to look at how the width of the patches affects the stress intensity factor. Analyses have been performed on a 200 mm crack with 6 mm CFRP patches with various overlap widths.

The study also looks at how the placement of the patches affects the results.

Figure 6.5 illustrates the different overlap configurations that have been analysed. (C) denotes that the overlap begins at the centre of the crack length.

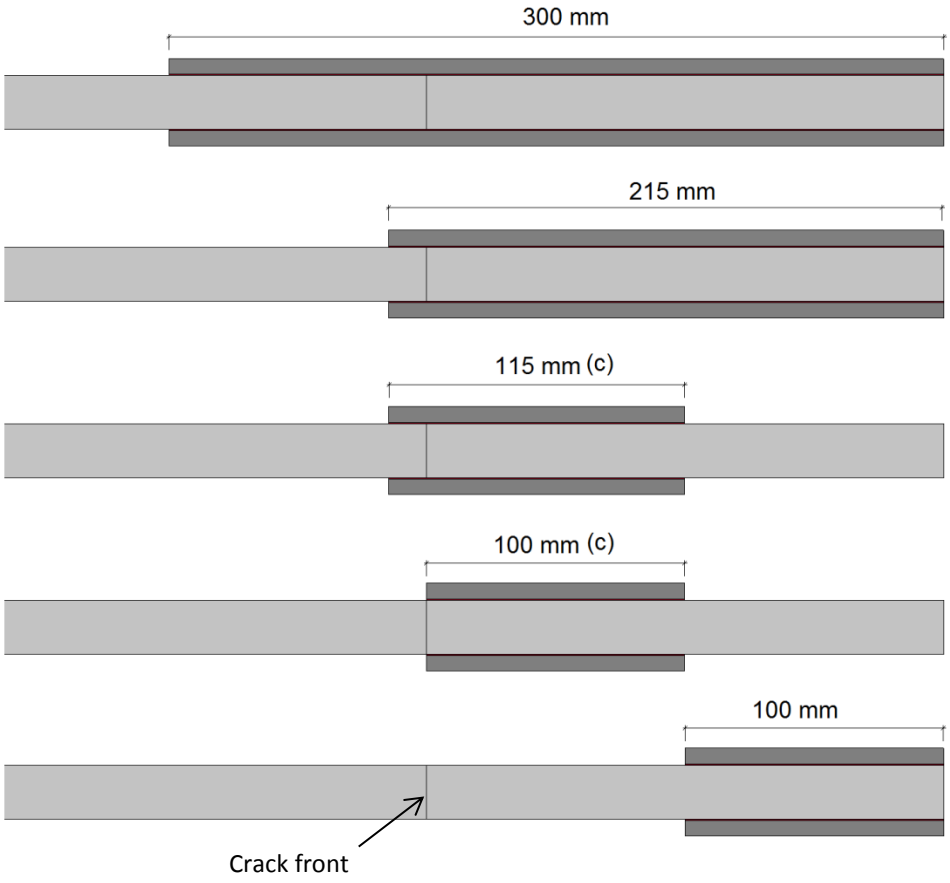

Figure 6.5: The crack plane of a 200 mm crack with different overlap configurations.

Table 6.2 presents *F* factors and stress intensity factors for the different overlap configurations. The table also lists the reduction of the stress intensity factor for the given overlap compared to a configuration with no patches. The results show that a decrease in overlap width, to a width that only covers half of the total crack length has relatively large impact on the patches' ability to reduce the stress intensity. The placement, however, of the 100 mm wide overlaps does not seem to effect the stress intensity factor to any significant extent. The configuration with the overlap that ends at

the centre of the crack length results in a larger stress intensity factor than the one that ends at the crack tip, but only by about 3 %.

Applying patches that covers an area beyond the tip of the crack shows little effect. It can be beneficial if the crack propagates further. The disadvantage may be the lack of visual control of the crack's rate of growth.

Table 6.2: *F* and *K* for a 200 mm crack with 6 mm patches with various overlap widths.

Crack length (mm)	**Overlap thickness** (mm)	**Overlap width** (mm)	**Load** MPa	**F**	***K*** $(\mathrm{MPa}\sqrt{m})$	**Reduction**
200	0	0	117,5	1,32	123,4	-
200	6	100	117,5	0,78	73,1	40,8 %
200	6	100 (c)	117,5	0,76	71,0	42,5 %
200	6	115 (c)	117,5	0,75	69,5	43,7 %
200	6	215	117,5	0,48	45,0	63,5 %
200	6	300	117,5	0,46	43,3	69,4 %

Patch capacity

It is also interesting to study how these different patch configurations affect the capacity of the joint. All the configurations from Figure 6.5 have therefore been loaded until failure; the nominal stress at failure for the different patches is presented in Table 6.3.

Table 6.3: Fracture loads for different overlap configurations.

Crack length (mm)	**Overlap thickness** (mm)	**Overlap width** (mm)	**Nominal stress at failure** MPa
200	6	100	241,8
200	6	100 (c)	250,7
200	6	115 (c)	253,7
200	6	215	256,1
200	6	300	258,0

Table 6.3 shows that the different patch configurations have little effect on the capacity. The failure loads differ by only 6.3 % from the 300 mm wide patches to the 100 mm wide patches.

Plots have been made in order to see if the patches have sufficiently long overlaps. Figure 6.6 displays plots of the shear stresses along the bondline of the 100 mm configuration at different loads until fracture initiates in the bondline at 341,8 MPa.

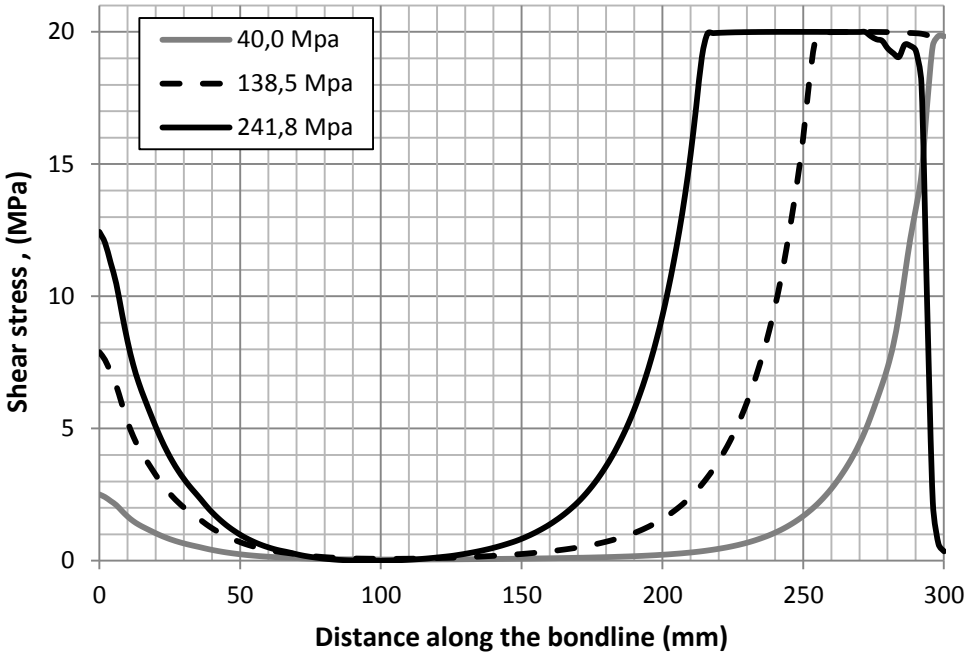

Figure 6.6: Shear stress along the bondline at different loads. 100 mm wide patch.

We can see that the bondline shear stresses are located at the ends of the overlap leaving the central part of the bondline unloaded. As the maximum shear stress at the right end reaches the yield stress, a plastic zone is developed. The length of this plastic zone increases with increasing loading until critical strain is reached and fracture is initiated at that end. This is consistent with the theory for long overlaps presented in Section 3.2.

6.1.4 Summary

A single-edge notched tension steel plate has been analysed with a number of different patch configurations. The results are in general promising; it is shown that the CFRP reinforcements effectively are able to reduce the stress intensity at the crack tip, thus limiting the severity of the crack. It is also seen that an increase in patch thickness from 3 mm to 6 mm led to a further reduction of the stress intensity factor by about 9 %.

When applying patches to real structures, achieving optimal design and placement of the patch repair can be challenging. It is shown, however, that it is highly advantageous if the patches can be applied in such a manner that they cover the whole length of the crack. If this is not to be achieved, the precise placement of the patch along the crack length is not of great importance. If the crack is

believed to propagate further, overlapping the crack tip to some extent would be preferable; if not, the stress intensity will increase as the crack grows at a much higher rate.

Although the results are in general promising, there are some limitations and possible sources of error.

Limitations of LEFM

One possible source of inaccuracy is the limitations of linear elastic fracture mechanics. As discussed in Section 2.6, an important restriction to the use of LEFM is that the size if this plastic zone at the crack tip must be small relative to the crack length as well as the geometrical dimensions of the specimen or part. Otherwise, fracture mechanics theory that includes nonlinear material behaviour is needed.

An overall limit on the use of LEFM was presented in Section 2.6, it states that LEFM is valid if

$$a, (W - a), h \geq \frac{4}{\pi}\left(\frac{K}{\sigma_{ys}}\right)^2 \tag{6.1}$$

To make sure the LEFM is adequate, Equation (6.1) is tested for the configuration with no patch, where the plastic zone is expected to be the largest. The results are presented in Table 6.4.

Table 6.4: Plasticity limitations on LEFM.

$\boldsymbol{a}$	$\boldsymbol{W-a}$	$\boldsymbol{h}$	$\boldsymbol{K}$	$\boldsymbol{\frac{4}{\pi}\left(\frac{K}{\sigma_{ys}}\right)^2}$
(mm)	(mm)	(mm)	$(\mathrm{MPa}\sqrt{m})$	(mm)
50	1450	2600	56,3	26
100	1400	2600	81,3	54
150	1350	2600	102,7	86
200	1300	2600	123,4	124
250	1250	2600	144,6	171

As we can see, Equation (6.1) is satisfied for all crack lengths, hence linear elastic theory is adequate.

Mode III influence

Another element that may cause some minor inaccuracy is the fact that the adhesive layers are to some extent experiencing Mode III loading. This is due to deformations in the steel plate, which causes shear stresses parallel to the crack plane in the adhesive layers. The critical energy release rate for Mode III fracture is unknown, and is therefore assumed to be equal to the critical energy release rate for Mode II.

The deformed plate is illustrated in Figure 6.7 with a deformation scale factor of 300, the CFRP patches and adhesive layers are hidden.

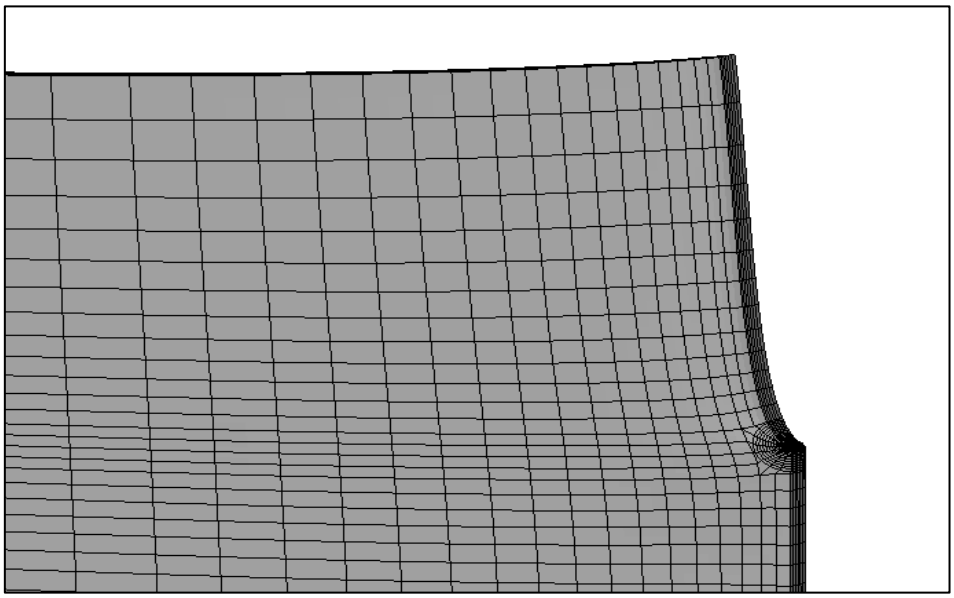

Figure 6.7: Deformation scale factor = 300

6.2 Fatigue life estimation for a crack emanating from a ship manhole

A manhole on the deck of a shuttle tanker, experiencing crack growth has been modelled and analysed in Abaqus, with and without CFRP reinforcement.

The main objective of the modelling was to estimate the amount of cycles (under constant amplitude loading) required for the crack to grow from its initial size a_i to a final size $a_{f,}$ with and without CFRP patches.

In the present section, results from the analyses will be presented and discussed. First, we will look at a configuration where patches have been placed on both sides of the deck, then a configuration with a patch inside the rim of the manhole.

At the end of this section, a short summary will be presented.

6.2.1 Double sided patch repair

In order to estimate the amount of cycles required for the crack to grow from its initial size, $a_i = 105$ mm, to its final crack length, $a_f = 400$ mm, the stress intensity range has been calculated for a number of crack lengths ranging from a_i to a_f. By using Paris Law the fatigue crack growth rate (*da/dN*), for the crack with and without patches, has been calculated for all the chosen lengths.

The inverted growth rate (cycles/mm) for the propagating crack is plotted in Figure 6.8, for both the configuration with CFRP patches, and without. The area beneath the "*dN/da* versus *a"* curve represents the total amount of cycles, N_{if}.

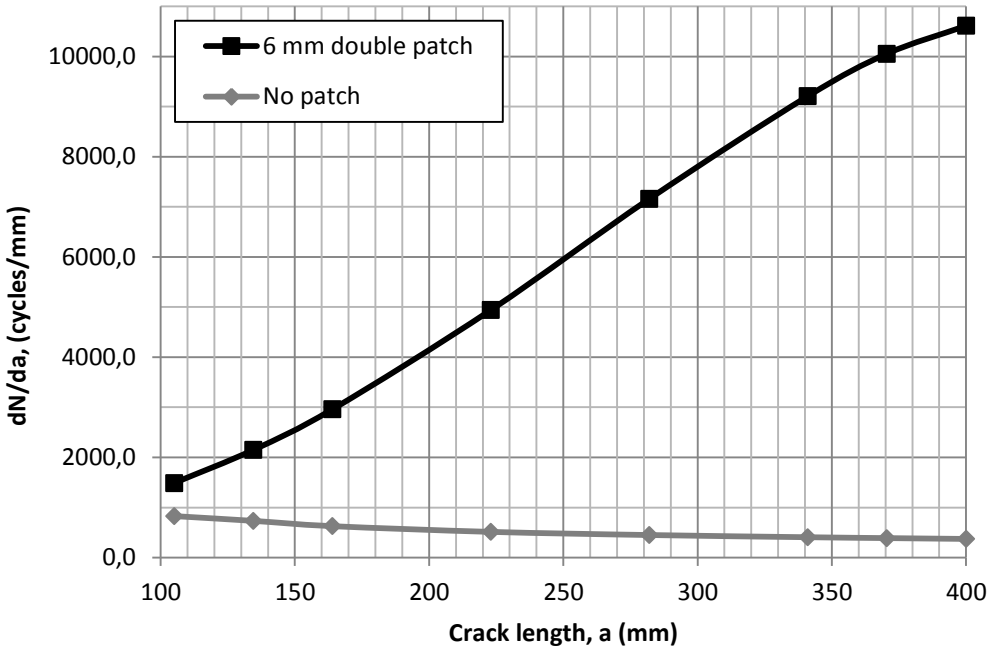

Figure 6.8: "*dN/da* versus *a*" curves.

The plot shows that for the configuration with no patch, the amount of cycles needed for the crack to grow a short increment, *da,* of the total crack length decreases as the crack grows. This due to the increasing stress intensity, in which escalates the growth rate.

For the configuration with the 6 mm double sided patch, the situation is just the opposite. The crack growth rate decreases as the crack propagates into the patched area and a larger part of the cracked deck is bridged. Hence, the amount of cycles needed to propagate the crack an increment, *da*, increase as the crack grows.

The area underneath the curves, which equals the total amount of cycles, is estimated using Simpson's rule (se Section 5.1.4). The results are presented in Table 6.5 for the configuration with no patch, and Table 6.6 for the double patched configuration.

Table 6.5: Life estimation of crack emanating from manhole - No patch

Crack length (mm)	Load (MPa)	F	K $(\mathrm{MPa}\sqrt{m})$	dN/da (cycles/mm)	Cycles
105	50	1,95	55,9	828,8	-
134,5	50	1,79	58,3	733,4	43167
164	50	1,71	61,4	627,6	-
223	50	1,57	65,6	513,7	61613
282	50	1,46	68,5	450,6	-
341	50	1,37	70,9	407,1	48225
400	50	1,30	73,0	373,0	-
				Sum (N_{if}):	**153 006**

Table 6.6: Life estimation of crack emanating from manhole - Double 6 mm CFRP patch

Crack length (mm)	Load (MPa)	F	K $(\mathrm{MPa}\sqrt{m})$	dN/da (cycles/mm)	Cycles
105	50	1,60	46,0	1488,2	-
164	50	1,02	36,6	2960,6	359345
223	50	0,74	30,9	4941,4	-
282	50	0,58	27,3	7159,3	841443
341	50	0,48	25,1	9206,8	-
370,5	50	0,45	24,3	10055,2	590396
400	50	0,43	23,9	10612,7	-
				Sum (N_{if}):	**1 791 184**

At an average fatigue stress range ΔS of 50 MPa, the life is estimated to 66 246 cycles for the unpatched deck and 959 769 cycles when it's mended with a 6 mm double sided CFRP patch. Thus, the patch repair has substantially increased the amount of cycles needed for the crack to reach the critical length.

The removal of the manhole's liner and its effect on K

The liner on top of the manhole was, in order to save computational costs, removed from the model. This reduction of the model does, however, have an effect on the stress intensity. A comparison between a model with and without a liner has been performed to control that the stress intensity factors was not influenced to an excessive degree. The 400 mm crack was chosen for the analyses and the results are presented in Table 6.7. The deck is loaded with a nominal stress of 50 MPa.

Table 6.7: Comparison of the stress intensity factors for models with and without the manhole liner.

Patch	No liner K $(\mathrm{MPa}\sqrt{m})$	Liner K $(\mathrm{MPa}\sqrt{m})$	Error
No patch	73.0	76.6	4.7 %
Double 6 mm patch	23.9	24.0	0.4 %

Including the liner in the model increases the stress intensity to some extent for the configuration without patches. For the configuration with patches, the difference is only 0,4 %. Excluding the liner, in other terms, leads to some underestimation of the severity of the crack when it's modelled without patches, which again means that the crack's lifetime is somewhat overestimated. The difference in lifetime presented in Table 6.5 and Table 6.6 may therefore, to some extent, be a conservative estimate.

6.2.2 Single patch repair inside rim

A life estimate has also been made for the configuration with a single patch inside the rim. The results are presented in Table 6.8.

Table 6.8: Life estimation of crack emanating from manhole - Single 6 mm CFRP patch inside liner.

Crack length (mm)	Load (MPa)	F	K $(\mathrm{MPa}\sqrt{m})$	dN/da (cycles/mm)	Cycles
105	50	1,86	53,4	954,1	-
134,5	50	1,68	54,7	884,6	104236
164	50	1,57	56,4	807,7	-
223	50	1,42	59,4	691,9	82290
282	50	1,32	62,0	609,0	-
341	50	1,24	64,3	544,7	32251
400	50	1,19	66,6	491,8	-
				Sum (N_{if}):	**218 777**

Figure 6.9 compares the inverted growth rate (cycles/mm) for both patch repair configurations.

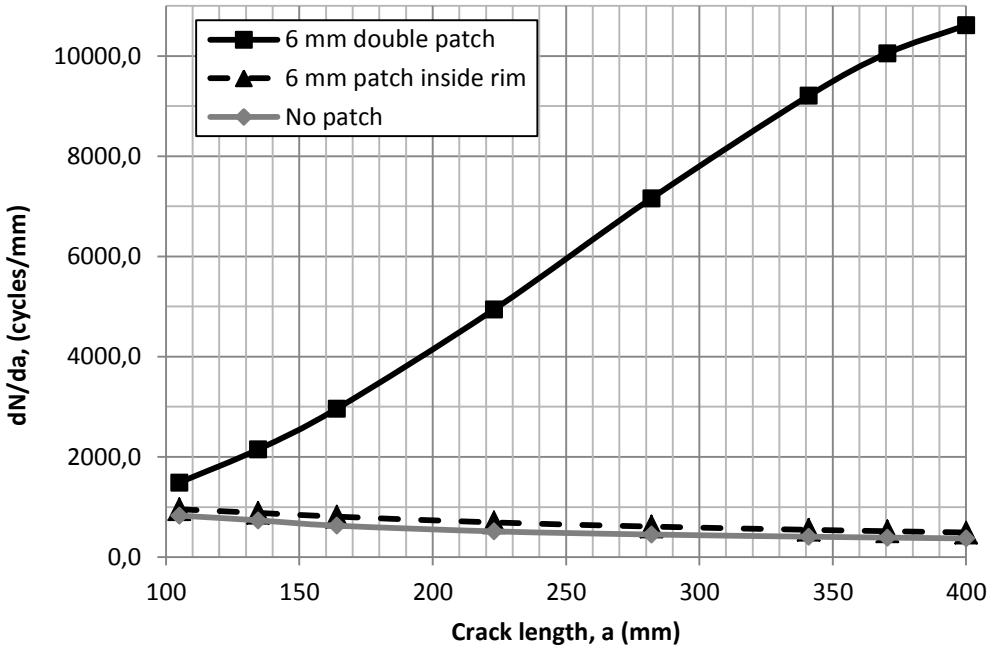

Figure 6.9: "*dN/da* versus *a*" curves for different overlap configurations.

As we can see, both from Table 6.8 and Figure 6.9, the single patch inside the rim does not have the same reducing effect on the stress intensity factors as the double sided patch. The crack growth rate of the configuration with the double sided patch decreases as the crack propagates in the patched area. The growth rate of the single patched configuration, however, escalates as the crack grows, which results in a much a shorter life expectancy.

Restraining the deck to prevent vertical movement – Effect on K

The whole surface underneath the deck is, for the given configuration, restrained from movement in the vertical direction. This additional boundary condition was assigned the model in order to prevent the deck from bending. Attempts were made to run the model without this extra restraint, but they were unsuccessful.

The model was able to run when modelled without the patch. With the objective to investigate how this extra constraint influences the stress intensity factors, a comparison was made between a model with this additional boundary condition and one without. The resulting stress intensity factors along the thickness of the plate are plotted in Figure 6.10. The configuration without the liner is also plotted to illustrate "normal" plate behaviour.

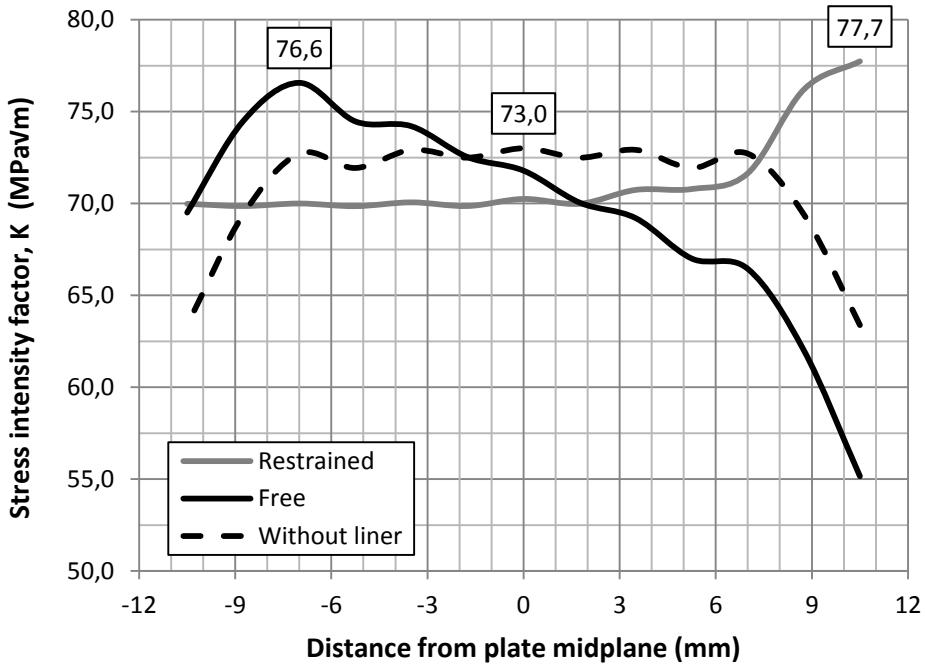

Figure 6.10: Stress intensity factors along the plate thickness.

The variation of the stress intensity along the thickness of the plate is quite different for the restrained and the “free” configuration, but the maximum stress intensity factors differ by only 1.4 %. There is no reason to believe that the difference would be significantly larger for the patched configuration, hence errors related to restraining the model are considered negligible.

6.2.3 Summary

Two patch repair configurations have been presented, a double sided patch and a single patch placed inside the rim of the manhole. The former has shown promising results by successfully bridging the deck together and reducing the stress intensity at the tip of the crack. The latter has to some extent been able to reduce the severity of the crack, but has failed to show the same limiting effect on the rate of crack growth as the double sided patch repair. The double sided patch were able extended the fatigue life of the crack with an extension factor of 11,7. The single patch with a factor 1,4.

Table 6.9 presents a summary of the stress intensity factors and life estimates for the different configurations.

Table 6.9: Comparison of *K* and N_{if} for different patch configurations.

Crack length (mm)	Load (MPa)	No patch K ($\mathrm{MPa}\sqrt{m}$)	Inside liner K ($\mathrm{MPa}\sqrt{m}$)	Double patch K ($\mathrm{MPa}\sqrt{m}$)
105	50	55,9	53,4	46,0
134,5	50	58,3	54,7	40,7
164	50	61,4	56,4	36,6
223	50	65,6	59,4	30,9
282	50	68,5	62,0	27,3
341	50	70,9	64,3	25,1
370,5	50	72,0	65,5	24,3
400	50	73,0	66,6	23,9
	N_{if}:	**153 006**	**218 777**	**1 791 184**

Limitations and uncertainties

Due to the simplification of the FE model of the manhole and the surrounding deck, the stress intensity is likely to be overestimated. Therefore, the final crack length of 400 mm is an arbitrarily selected length, and not governed by the material fracture toughness. For the configuration with double sided CFRP reinforcements, the crack growth rate is decreasing as the crack propagates. Hence, the majority of the cycles are accumulated at the last section of the total crack length, near a_f. For the unpatched configuration and the alternative with the single patch, most of the cycles are accumulated near the initial crack length, a_i. As a result, the choice of final crack length has a considerable impact on the life estimates. If the selected final crack length, a_f, was shorter, the difference in expected fatigue life would be less significant.

The fatigue life estimates are based on just 7 points on each "*dN/da* versus *a*" curves, separated with an interval Δ*a* = 59 mm (and 29,5 mm). The accuracy of the estimations would be higher if shorter intervals were chosen, but for each extra point another FE model is demanded. Hence, increasing the accuracy would be fairly time consuming and did not seem necessary for the given situation.

As with the SENT steel plate, another possible source of error is the limitations of linear elastic fracture mechanics. To make sure the LEFM is adequate in this instance as well, Equation (6.1) has been tested for the configuration with no patch. The results are presented in Table 6.10.

Table 6.10: Plasticity limitations on LEFM.

a	$W-a$	h	K	$\frac{4}{\pi}\left(\frac{K}{\sigma_{ys}}\right)^2$
(mm)	(mm)	(mm)	$(\mathrm{MPa}\sqrt{m})$	(mm)
105	2395	3900	55,9	32
134,5	2365,5	3900	58,3	34
164	2336	3900	61,4	38
223	2277	3900	65,6	44
282	2218	3900	68,5	47
341	2159	3900	70,9	51
370,5	2129,5	3900	72,0	52
400	2100	3900	73,0	54

As we can see, Equation (6.1) is satisfied for all crack lengths, hence linear elastic theory is adequate.

Another element that has a substantial impact on the life estimates are the Paris Law (Eq. (2.13)) material constants, *C* and *m*. And especially the value of *m* as it indicates the degree of sensitivity of the growth rate to stress. In our case when *m* = 3, doubling the stress range Δ*S,* which doubles the stress intensity range Δ*K,* increases the growth rate by a factor of $2^m = 8$.

When selecting the material constants, *C* and *m*, we also need to choose an appropriate *R*-ratio ($S_{min}/S_{\max}$), which is another parameter that affects the crack growth rate. Generally, an increase in *R* results in an increase in growth rates for a given stress intensity range (Dowling, 2012). *C* and *m* chosen in the present thesis apply for $R \approx 0$, zero-to-tension loading. This is a conservative choice as the wave induced loading is likely to cause a negative R-ratio.

The choices that have been made in the present thesis regarding the mentioned material constants, average stress range, *R*-ratio and crack length; have had a significant impact on the obtained results, and some of these choices may be debatable. The main objective of the present thesis is, however, to obtain results that are comparable, and in such circumstances, these choices become less critical as long as they are consistent. So even though some uncertainties may exist, key trends regarding the performance of the CFRP patches can be identified based on the presented results.

Chapter 7

Conclusion

The main objective of the present thesis was to study how composite patches can reduce the stress intensity in cracked steel plates, and how these patches, by reducing the stress intensity, can limit the extent of fatigue crack growth.

Two different cases have been analysed using the finite element software Abaqus; a single-edge notched tension steel plate and a ship manhole experiencing fatigue crack growth. The former has been modelled and analysed with a number of patch configurations with varying thickness, width and placement along the crack line. The latter has been modelled and analysed with two patch repair alternatives; first, with double sided CFRP strengthening of the cracked deck and then a single CFRP patch inside the rim of the manhole. For both alternatives fatigue life calculations has been made.

Based on the limited tests and analyses presented in this thesis, the following observations can be made. The parametric study of the SENT steel plate has shown that CFRP patches to a great extent are able to reduce the stress intensity at the tip of the crack. Additionally, it is shown that the composite thickness and especially the width have considerable influence on the performance of the patches. Analyses show that patches that only covers half the crack length has a significantly lower effect on the stress intensity, then patches that covers the whole length of the crack. The location of these patches along the crack does, however, not seem to affect the stress intensity factor to a large extent.

Applying patches that covers an area beyond the tip of the crack shows little effect on the stress intensity. Overlapping the crack tip is, however, highly recommendable if the crack is believed to propagate further. The crack growth rate will then remain at a low level. If a crack is able to propagate past a reinforced area, the growth rate will escalate as the crack grows, which is unfortunate. Covering the tip of the crack is in some circumstances unwanted as it makes it difficult to inspect and follow the growth of the crack. Another element of major importance is the length of the patch; long overlap length is needed in order to utilize the full potential of the CFRP reinforcements.

The fatigue life estimates of the manhole, has shown that the doubled sided CFRP strengthening of deck were able to extend the fatigue life of the crack with a factor of 11,7. The single patch inside the rim did not demonstrate the same reducing effect on the stress intensity, and was only able to extend the fatigue life by a factor 1,4.

The crack growth rate of the double sided patch configuration decreases as the crack propagates in the patched area. The growth rate of the single patch configuration, however, escalates as the crack grows, which results in a much a shorter life expectancy. This patch repair configuration is therefore not recommendable.

The results presented in the present thesis shows that composite patch repair solutions are, when applied in the right manner, well suited for preventing fatigue crack growth and extending the fatigue life of cracked plates.

The study in this thesis has mainly been focused on double sided reinforcement and Mode II fracture in the adhesive layers, but applying double sided patches and ensuring Mode II loading are not always possible. Access is often challenging, and there is not always sufficient space for an optimal patch placement. Further research on single sided patch repair and mixed mode fracture are therefore needed.

References

Adams, R. D., Comyn, J. & Wake, W. C., 1997. *Structural Adhesive Joints in Engineering.* 2. ed. London: Chapman & Hall.

Adams, R. D., Fay, P. A., Comyn, J. & Watts, J. F., 2005. *Adhesive bonding - Science, technology and applications.* Cambridge: Woodhead Puplishing.

Anderson, T. L., 2005. *Fracture Mechanics; Fundamentals and Applications.* 3. ed. Boca Raton, FL: CRC Press.

ASTM Int., 2008. *ASTM A131/A131M:08 - Standard Spesification for Structural Steel for Ships,* s.l.: ASTM.

Bakker, A., 1992. Three Dimensional Constraint Effects on Stress Intensity Distributions in Plate Geometries with Through-thickness Cracks. *Fatigue & Fracture of Engineering Materials & Structures,* Issue vol. 15.11, pp. 1051-1069.

Barsom, J. M. & Stanley, T. R., 1999. *Fracture and Fatigue Control in Structures: Applications of Fracture Mechanics.* 3rd ed. West Conshohocken, PA: ASTM.

Dassault systèmes, 2012. *Abaqus 6.12 online documentation.* Providence, RI, USA: Dassault systèmes Simulia Corp.

Dowling, N. E., 2012. *Mechanical Behavior of Materials; Engineering Methods for Deformation, Fracture, and Fatigue.* 4th ed. Harlow: Pearson Education.

eFunda, 2012. *eFunda.* [Online] Available at: http://www.efunda.com/formulae/solid_mechanics/fracture_mechanics/fm_lefm_modes.cfm#ModeI [Accessed 24.10.2012 October 2012].

Guthu, G. O., 2010. *Modelling of Mechanical Response and Fracture in Adhesively Bonded Joints,* Oslo: Faculty of Mathematics and Natural Sciences, University of Oslo.

Hart-Smith, L. J., 1973. *Ashesive-bonded double-lap joints,* Hampton, VA: NASA.

Hashim, S. et al., 2009. *Design and analysis of DLS steel/composite thick-adherend adhesive joints,* Edinburgh: 17th International Conference on Composite Materials (ICCM-17).

Lienhard, J. H., n.d. *University of Houston; The Engines of Our Ingenuity.* [Online] Available at: http://www.uh.edu/engines/epi1525.htm [Accessed 21 march 2013].

McGeorge, D., 2010. Inelastic fracture of adhesively bonded overlap joints. In: A. R. Ingraffea & K. -. Schwalbe, eds. *Engineering Fracture Mechanics.* s.l.:Elsevier.

McGeorge, D., 2012. Predicting the failure of bonded structural joints in marine engineering. In: J. R. Weitzenböck, ed. *Adhesives in marine engineering.* Cambridge: Woodhead Publishing, pp. 72-96.

Osnes, H. & Guthu, G. O., 2011. Strength of bonded overlap composite joints for marine applications. In: P. Camanho & L. Tong, eds. *Composite joints and connections: Principles, modelling and testing.* Cambridge: Woodhead Publishing, pp. 399-422.

Paris, P. C. & Sih, G. C., 1964. Stress Analysis of Cracks. In: *Fracture Toughness Testing and Its Applications.* Chicago: ASTM International, pp. 30-83.

Rotwitt, P. B., 2012. *Modelling of adhesively bonded joints,* Oslo: s.n.

Tada, H., Paris, P. C. & Irwin, G. R., 2000. *The stress analysis of cracks handbook.* 3d ed. ed. New York: ASME Press.

Tsai, M. Y., Oplinger, D. & Morton, J., 1998. Improved theoretical solutions for adhesive lap joints. *International Journal of Solids and Structures vol. 35*, April, p. 1163–1185.

Weitzenböck, J. R., 2012. Introduction to using adhesives in marine and offshore engineering. In: J. R. Weitzenböck, ed. *Adhesives in marine engineering.* Cambridge: Woodhead Publishing, pp. 1-16.

Y. Yamamoto, Y. S., 1978. Stress intensity factors for three-dimensional cracks. *International Journal of Fracture ,* February, Issue Volume 14, Issue 1, pp. 17-38.